RSC Advances

PAPER

View Article Online
View Journal | View Issue

Cite this: *RSC Adv.*, 2019, **9**, 40977

Enhanced mechanical properties of hBN–ZrO_2 composites and their biological activities on *Drosophila melanogaster*: synthesis and characterization†

Amarendra Gautam,[a] Chandkiram Gautam,[*a] Monalisa Mishra,[b] Vijay Kumar Mishra,[c] Ajaz Hussain,[a] Swetapadma Sahu,[b] Reetuparna Nanda,[b] Bikash Kisan,[b] Santoshkumar Biradar[d] and Rakesh Kumar Gautam[e]

In this study, six compositions in the system [x(h-BN)–(100 − x)ZrO_2] (10 ≤ x ≤ 90) were synthesized by a bottom up approach, *i.e.*, the solid-state reaction technique. XRD results showed the formation of a novel and main phase of zirconium oxynitrate $ZrO(NO_3)_2$ and SEM exhibited mixed morphology of layered and stacked h-BN nanosheets with ZrO_2 grains. The composite sample 10 wt% h-BN + 90 wt% ZrO_2 (10B90Z) showed outstanding mechanical properties for different parameters, *i.e.*, density (3.12 g cm^{-3}), Young's modulus (10.10 GPa), toughness (2.56 MJ m^{-3}), and maximum mechanical strength (227.33 MPa). The current study further checked the *in vivo* toxicity of composite 10B90Z and composite 90B10Z using *Drosophila melanogaster*. The composite 10B90Z showed less cytotoxicity in this model, while the composite 90B10Z showed higher toxicity in terms of organ development as well as internal damage of the gut mostly at the lower concentrations of 1, 10, and 25 μg mL^{-1}. Altogether, the current study proposes the composite 10B90Z as an ideal compound for applications in biomedical research. This composite 10B90Z displays remarkable mechanical and biological performances, due to which we recommend this composition for various biomedical applications.

Received 26th September 2019
Accepted 25th November 2019

DOI: 10.1039/c9ra07835e

rsc.li/rsc-advances

1. Introduction

Increasing interest in the development of advanced composites for various biomedical applications has impelled a large amount of research to synthesize easily scalable, low-density, high-strength, wear-resistant and non-toxic biomaterials. The elemental dullness with low density pooled with high strength makes h-BN one of the capable materials for these applications. Boron (B) and nitrogen (N) atoms are bonded with strong covalent bonding, whereas weak van der Waals forces bind the layers, which allow the layers to glide next to each other simply. This special sparkler arrangement and unique bonding between as well as distinctive performances such as proportional elemental and thermal dullness, mechanical properties, hardness and strength, good corrosion resistance and stability at high temperatures, brilliant electrical lagging properties and good manufacturability make h-BN promising for various applications.[1–12] Recently, three dimensional (3-D) interrelated nanostructures of h-BN and graphene architectures were synthesized using numerous novel methods.[13–18] Hence, it is predictable that the growing 3-D h-BN architectures will enhance their significance in a wide range of applications.[19,20] Owing to the heterostructures and similarity with carbon, h-BN represents elevated thermal resistance and high mechanical strength.[21–25] The surprising performance of h-BN provides a novel material for the production of numerous technological applications. h-BN-based bioceramics with good chemical stability and high oxidation resistance have been used in diverse research areas at a large scale such as metallic and chemical industries and thermal security systems.[26–32]

ZrO_2 is still being employed as a biomaterial for various implants; however, owing to high brittleness, it undergoes terrible failure when a load is applied beyond a certain limit.[33,34] Hence, scientists are much attracted towards the development of such ZrO_2-based novel composites, which reveals relatively high mechanical properties and low density with notable

[a]*Advanced Glass and Glass Ceramics Research Laboratory, Department of Physics, University of Lucknow, Lucknow-226007, India. E-mail: gautam_ceramic@yahoo.com; Tel: +918840389015*

[b]*Neural Developmental Biology Lab, Department of Life Science, National Institute of Technology, Rourkela, Odisha-769008, India*

[c]*Department of Physics, Faculty of Science, Banaras Hindu University, Varanasi - 221005, UP, India*

[d]*Department of Materials Science & Nano Engineering, Rice University, Houston, Texas, USA*

[e]*Department of Mechanical Engineering, Indian Institute of Technology, Banaras Hindu University, Varanasi - 221005, UP, India*

† Electronic supplementary information (ESI) available. See DOI: 10.1039/c9ra07835e

biological performances for bone implant applications. However, plentiful investigations have been carried out in the research field of biocomposites for numerous biomedical applications such as in jawbone, joint, hip, and dental implants but the stability and biocompatibility of these implants are not adequate due to their high density, highly fragile nature, high coefficient of thermal expansion, and low resistance to corrosion with respect to acid and humid environments.[35–42]

Hence, scientists having enormous interest for the fabrication of new biocomposites such as zirconia doped alumina, ceria/yttria stabilized zirconia (Ce/Y-TZP), and $84ZrO_2$–$8Al_2O_3$–$8SrAl_{12}O_{19}$, which show notable mechanical strength, stiffness, venerable biocompatibility, and substantial requirements for several dental/bone implant appliances.[43–50] Recently, three dimensional nanostructured biocomposites of hBN–B_2O_3 were fabricated using plasma sintering technique for bone restoration applications and 3-D interconnected architecture of h-BN reinforced ZrO_2 composites for structural evolution and enhanced mechanical properties of bone implant applications.[18,51] They found remarkable osteogenic properties with enough compressive strength. Besides the mechanical fidelity, they also report pretty good chemical stability and biocompability. Initially, in 1969, ZrO_2 was used for medical devices in biomedicine as an innovative implant for head, knee, and jaw/teeth in dentistry owing to superior mechanical characteristics.[52–54] Due to the high utility, its efficacy and malicious effects on humans is a matter of concern. Animal studies have revealed the toxicity of zirconia nanoparticles in zebra fish and *Drosophila*.[55,56] *Drosophila melanogaster* is used as a model to test the toxicity of various nanoparticles[57,58] because of its short natural life, simple translucent larval structure, small size, ease of handling, and ease of visualization under a microscope. The evolutionary conserved diseased genes can be used to check the toxic effect in the current study.

In this study, we intend the preparation of composites of h-BN and ZrO_2 through a simple solid-state reaction to obtain better malleability and improvement in the mechanical and tribological properties without varying the other properties, using a typical sintering method for biomedical applications.

2. Materials and methods

2.1. Fabrication of hBN–ZrO_2 samples

Herein, various novel composites were synthesized by investigative AR grade chemicals, hexagonal boron nitride (h-BN) (Sigma Aldrich, purity 99%), and zirconia (ZrO_2) fine particles (Tosoh Corp. Japan, 27 nm). Total six compositions of h-BN and ZrO_2 powders depending on the ratio of their amounts in wt% as (i) 10 wt% h-BN + 90 wt% ZrO_2 termed as 10B90Z, (ii) 20 wt% h-BN + 80 wt% ZrO_2 termed as 20B80Z, (iii) 40 wt% h-BN + 60 wt% ZrO_2 termed as 40B60Z, (iv) 60 wt% h-BN + 40 wt% ZrO_2 termed as 60B40Z, (v) 80 wt% h-BN + 20 wt% ZrO_2 termed as 80B20Z, and (vi) 90 wt% h-BN + 10 wt% ZrO_2 termed as 90B10Z, were synthesized by mixing them carefully into acetone as the liquid media for 6 h using an agate mortar and pestle. The homogeneously mixed and dehydrated reactant powders of the above mentioned compounds were taken into six different alumina crucibles, which were finally kept into a fully programmable furnace having silicon carbide (SiC) as the heating element used for calcinations at 650 °C @ 5 °C m^{-1} for 1 h to remove the volatile impurities from the material. In this way, the desired bright white material was obtained. The various cylindrical pellets of the obtained dried powders were prepared under an optimized load of 10 ton using a vertical hydraulic press machine at room temperature. The cylindrical pellets were further heated for sintering at 1000 °C @ 5 °C m^{-1} for 3 h into a Metrex made automatic electric furnace. Thus, the obtained composite samples were then examined for the several concerned characterizations, *i.e.*, structural, morphological, mechanical, tribological, and biological investigations.

3. Sample characterizations

In order to examine the crystallographic structures of the composites, *viz.*, 10B90Z, 20B80Z, 40B60Z, 60B40Z, 80B20Z, and 90B10Z, the XRD patterns were obtained within the range of 15–60° 2θ values at the scanning rate of 3° min^{-1} by employing Rigaku Miniflex-II XRD consisting of Cu-Kα radiation having the wavelength, $\lambda = 0.15418$ nm, monitored at 40 kV and 40 mA. The density values of the sintered composites were evaluated by using a mass/volume formula.

The respective amounts of all the powder samples were mixed with potassium bromide in weight fraction of 1 to 99 using mortar and pestle. Further, various uniformed and cylindrical pellets having diameter of 12 mm were shaped and dried at 120 °C for 60 min in an oven. Finally, IR spectroscopic measurements were performed to understand the bonding mechanisms and interaction between the constituent molecules of the fabricated composites within the wavenumber range from 4000–400 cm^{-1} using an IR Affinity-1S spectrometer (Shimadzu). Raman spectroscopic studies were also carried out using a Renishaw In-Via Reflex Micro-Raman spectrometer having a 514.5 nm Argon laser. To analyze the surface composition and chemical states of the composite sample, X-ray photoelectron spectroscopy was performed using PHI-5000C ESCA Versaprobe-II, FEI, Inc., with Al KR X-ray as the excitation source. A BET analyzer (BELSORP-MINI-II, Japan Inc.) was employed to investigate the surface area and average pore diameter under nitrogen gas adsorption–desorption.

To obtain the surface morphological information from the sintered, polished, and Ag–Pd coated composite pellets, SEM was performed using a scanning electron microscope (JEOL JSM-6400). The coating on the pellet samples was done by an Auto Fine Coater sputtering machine (JEOL, JEC-3000FC). Eventually, the coated samples were then fixed upon the copper stubs by conducting carbon tape and the SEM images were recorded at appropriate magnifications.

To analyze the particle shape and size of the composite, transmission electron microscopy was also conducted by a field emission gun electron microscope (JEOL 2100). A fraction of milligram of the powder sample 10B90Z was subjected to bath sonication up to 25 min in $CH_3CHOHCH_3$. Further, few tiny

drops were cast on the top surface of the holey carbon grid and then dried in a vacuum chamber for 24 h. Thus, the TEM images were recorded for the vacuum dried sample.

For mechanical characterisation, the Universal Testing Machine (Instron 3639) was employed in the compression mode for the sintered pellets (diameter and height 1.2×1.2 cm^2). The load bearing capability of all the samples was investigated by stress–strain curves, using which the Young's modulus and fracture toughness were determined. The fracture toughness values were estimated using the area under the stress–strain curves.

The wear and sliding friction tests were performed using a pin-on-disk apparatus (Magnum Engineers, Bangalore, India). A rotating disk of EN31 steel hardened to 60 HRC was also utilized as a counter face for testing the composite pins, which were fixed during the measurements. The load was applied to the pin through the lever, resulting in a continuous contact between the pin and the counter face. Moreover, the wear tests were performed for a total duration of 800 seconds and then the weight loss was determined using an analytical balance having 0.0001 g accuracy. Three tests were performed for each composite under the same environment. The machine associated with a control panel reveals the frictional force and therefore, the friction force was noted after every 30 s and the same method was used to calculate the coefficient of friction.

3.1. Fly stock maintenance

Control *Oregon-R* flies were used to check the toxic effects of the composite samples. The stock was provided by C-CAMP, Fly Facility Bengaluru India. The flies follow a generalized short period of lifecycle of 10–15 days, which allows us to study all the positive and negative effects of the nanoparticles. They were fed with regular fly food, which consisted of corn meal, yeast powder, sucrose, and agar–agar type I. The fabricated nanocomposites were fed to the flies by mixing them in their food with their respective concentrations. Five different concentrations were chosen to check the toxicity of the nanocomposites 10B90Z and 90B10Z, *i.e.*, 1 μg mL^{-1}, 10 μg mL^{-1}, 25 μg mL^{-1}, 50 μg mL^{-1}, and 100 μg mL^{-1}, along with the control. All the vials having these flies were reared with 12 h light–dark conditions at 25 °C.

3.2. Developmental cycle analysis

The life cycle of *Drosophila* was tested from the egg to the adult stage of development at an interval of 6 h and was compared with the control to check any delay in the developmental stages. All the developmental changes of the fly were carefully observed. The number of pupa was observed in each vial for three days after pupa formation at an interval of 24 h and they were compared with the control.

3.3. Larval crawling assay

Wild type larvae or the control larvae choose to crawl in a straight line towards the periphery of the plate; however, the treated larvae or the larvae with some defects generally take a longer path by stopping and changing their direction multiple times. This assay was done by following Mishra and Barik's study.[59] Briefly, third instar larvae were collected from the food vials and washed in 1× PBS (phosphate buffer saline) to get rid of the extra amount of particulate food stuck on their body. Then, they were allowed to move over a 2% solidified agar gel prepared in a 90 mm petri dish. The trailing path of the larvae was marked. To check the distance travelled by the larvae, we put a graph paper below the petri dish and recorded the speed of the larvae for 1 min. The speed was determined by counting the number of squares travelled by the larvae within 1 min. A graph was plotted using the distance travelled by the larvae.

3.4. Trypan blue staining

To verify the dead cells inside the gut tissue of *Drosophila*, trypan blue staining was done after feeding with the composite samples. Any kind of injury in the tissue allows trypan blue to enter through its membrane and get attached to the damaged cells, thus giving blue colour to that area. In this way, the live cells can be distinguished from the dead cells. Trypan blue staining was done by following the study by Mishra *et al.*[56] Briefly, six third instar larvae were taken from each concentration along with the control to perform this assay. One wash with PBS was done prior to staining. 0.5 mg mL^{-1} of trypan blue (HIMEDIA) was used to stain the larvae for 30 minutes in dark. After incubating with the stain, the larva were rewashed with PBS and then observed under a stereo microscope.

3.5. Nitro blue tetrazolium (NBT) reduction assay for reduced oxygen species (ROS) production

ROS production is the result of a normal metabolic pathway that maintains homeostasis in one organism. NBT assay is performed to analyze the amount of free radical yield inside the larvae after treatment with the nanocomposite. The NBT test was performed by following the method reported by Mishra *et al.*[56] Briefly, the haemolymph was extracted in ice-cold temperatures in order to avoid melanisation. For the extraction of the haemolymph, 15 larvae of all concentrations were pinched by means of a sterilized needle in a micro centrifuge tube of 0.5 mL with a small cut at its base. The tube was kept in a tube of 1.5 mL and centrifuged at 4 °C in 6000 rpm for 5 min to collect the larval haemolymph. Then, to the 1.5 mL tube, 10 μL of 1× PBS was added. 10 μL of NBT was added to the tube and the sample was kept in dark for 1 h at room temperature. Then, 20 μL of acetic acid glacial (100%) was mixed with the sample and incubated for 5 min. Finally, 150 μL of acetic acid glacial (50%) was mixed with it. After mixing properly, the sample was taken in a 96 well plate to check the OD at 595 nm.

3.6. Adult phenotype assay

The fly grew on nanocomposite mixed food and laid eggs in the vial. The embryo completed the developmental stages and the first generation fly (F1) was enclosed. 50 adult flies were taken

from each of the different concentrations along with the control. They were anesthetized and observed carefully under the digital stereo microscope for unusual phenotypic defects in any body part with special reference to thorax, eyes, and wings. The arrangement of ommatidia in each eye was observed. The wings were placed over slides and scanned under a digital stereo microscope to check defects in the venation patterns. For the thorax, the number of bristle pairs was counted from the images and searched for abnormal pattern of bristle. Any phenotypic concentration of the flies were recorded and plotted in the graph.

4. Results and discussion

4.1. XRD analysis

XRD patterns of the prepared nanocomposites of hBN–ZrO_2 were recorded and are depicted in Fig. 1(a–f). The diffraction peaks were sharp for all the compositions and found to be slightly shifted towards higher angle side with increasing concentration of h-BN. A high intensity characteristic peak was observed at 2θ value ~28.32° that confirmed the formation of the major phase of zirconium oxynitrate [$ZrO(NO_3)_2$] (JCPDS file no. 049-1062). The secondary phase formation of zirconium boride ($B_{12}Zr$) (JCPDS file no. 044-1081), hexagonal boron nitride (h-BN) (JCPDS file no. 035-1365), and zirconium nitrite (Zr_2ON_2) (JCPDS file no. 050-1170) were also confirmed and marked in their respective XRD patterns.

4.2. Infrared spectroscopic analysis

In order to study the mechanisms of bond formation, FTIR measurements of the pure h-BN, pure ZrO_2, and their nanocomposites were performed and the results are shown in Fig. S1(a, b)† and Fig. 2(a–e) respectively. Fig. 2(a–e) depicts the IR spectra recorded for (a) 10B90Z, (b) 20B80Z, (c) 60B40Z, (d) 80B20Z, and (e) 90B10Z. The different shoulders that appeared in the IR spectra of various h-BN–ZrO_2 nanocomposites are represented in Table 2 and their assignments are given in Table 5. The peaks are shown in a rising sequence of 1 to 15. The IR spectra exposed different distinctive absorption peaks that confirm the existence of different stretching and bending vibrational modes of h-BN and ZrO_2. The asymmetric stretch of N–B–N appears in the wavenumber range from 1383–1490 cm^{-1}; however, the same vibration for B–N–B appeared in the wavenumber range from 767–775 cm^{-1}.[60–62] The absorption bands (1) and (2) arose due to the presence of ZrO_2 in the

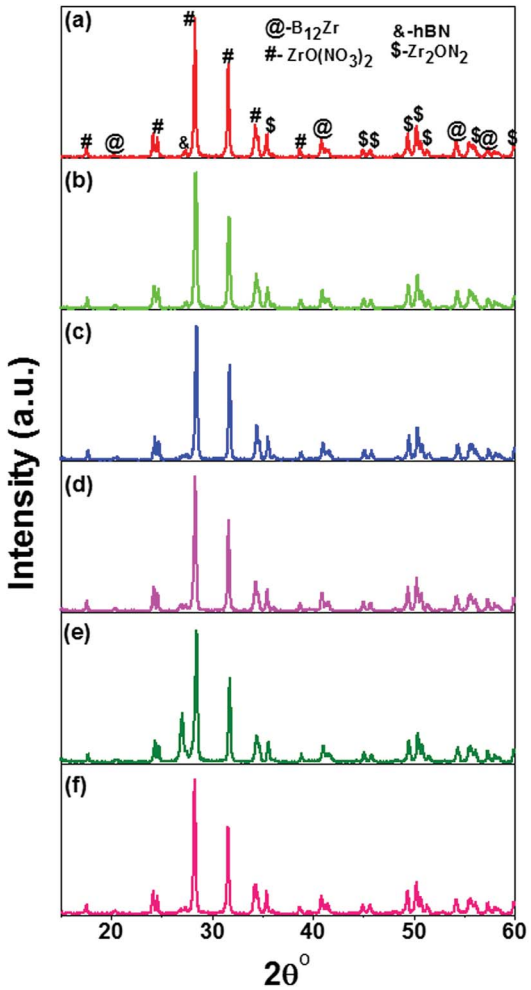

Fig. 1 XRD patterns of the prepared hBN–ZrO_2 biocomposite of (a) 10B90Z, (b) 20B80Z, (c) 40B60Z, (d) 60B40Z, (e) 80B20Z, and (f) 90B10Z sintered at 1000 °C for 3 h.

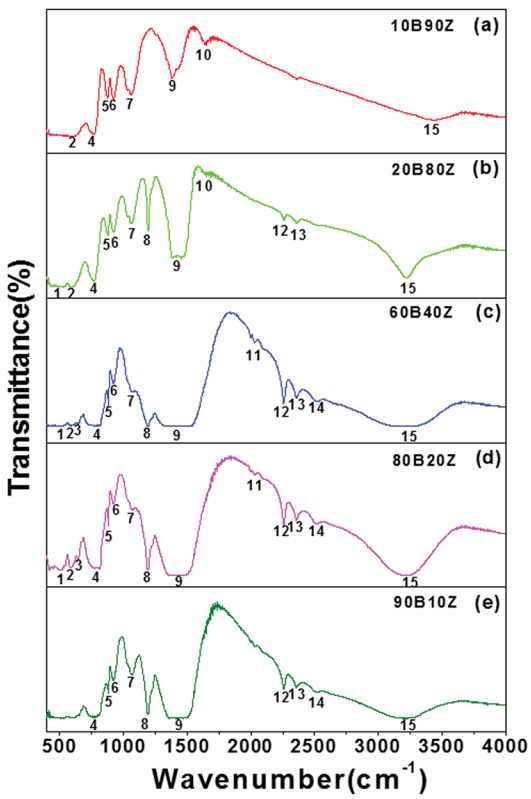

Fig. 2 IR spectra of the prepared hBN–ZrO_2 composite samples (a) 10B90Z, (b) 20B80Z, (c) 60B40Z, (d) 80B20Z, and (e) 90B10Z sintered at 1000 °C for 3 h.

Table 1 Sample code, h-BN compositions, density, mechanical strength, Young's modulus, toughness, surface area, pore size and pore volume for all the composite samples

Sample code	BN compositions (%)	Density ($g\ cm^{-3}$)	Mechanical strength (MPa)	Young modulus (GPa)	Toughness ($MJ\ m^{-3}$)	Surface area ($m^2\ g^{-1}$)	Pore size (nm)	Pore volume ($cm^3\ g^{-1}$)
10B90Z	10	3.12	227	10.10	2.56	21.011	1.21	3.71
20B80Z	20	3.04	129	9.93	0.96	—	—	—
40B60Z	40	2.82	95	6.60	0.57	—	—	—
60B40Z	60	2.79	76	5.44	0.53	31.073	1.64	7.63
80B20Z	80	2.70	38	3.70	0.45	—	—	—
90B10Z	90	2.67	34	3.57	0.16	65.666	1.66	12.24

Table 2 Composite samples code, peak positions in IR spectra of all the composite samples

	IR peaks position (cm^{-1})														
Samples code	1	2	3	4	5	6	7	8	9	10	11	12	13	14	15
10B90Z	—	—	—	767	876	923	1060	—	1383	1634	—	—	—	—	3451
20B80Z	—	590	—	769	882	923	1060	1194	1386, 1456	1627	—	2258	2358	—	3221
60B40Z	—	590	643	769	884	922	1071	1193	1338, 1517	—	2030	2257	2358	2515	3242
80B20Z	507	586	646	814	884	923	1072	1193	1366, 1487	—	2032	2257	2358	2515	3199
90B10Z	—	—	—	775	883	922	1066	1193	1361, 1490	—	—	2257	2358	2515	3223

wavenumber range from 0–07 cm^{-1} and 586–590 cm^{-1}, respectively; however, bands (3) and (4) occurred in the wavenumber range from 643.28–646.18 cm^{-1} and 767–814.95 cm^{-1}, respectively, band (5) in the wavenumber range from 876–883 cm^{-1}, band (6) in the wavenumber range from 922–923 cm^{-1}, and band (7) in the wavenumber range from 1060–1072 cm^{-1} (h-BN vibrational modes) occurred due to the presence of h-BN.[63] The peak (8) situated at 1193 cm^{-1} might be represent the B–O–H bending vibrations.[18] Further, a high intensity band (9) that appeared in the wavenumber range from 1338–1386 cm^{-1} and 1456–1517 cm^{-1} is associated with the B–N stretching vibrations and B–O, respectively.[64] In Fig. S1(b),† a strong thick envelop in the wavenumber range from 1386–1456 cm^{-1} was observed that could be attributed to the very close involvement of both h-BN as well as ZrO_2 vibrations. The absorption band (10) appeared due to ZrO_2. The absorption bands (11), (12), (13), and (14) occur at different wavenumber ranges from 1627–1634 cm^{-1}, 2030–2032 cm^{-1}, 2257–2258 cm^{-1}, 2358 cm^{-1}, and 2515 cm^{-1}, which appeared owing to h-BN correspondingly. Fascinatingly, as the concentration of h-BN was increased, the absorption bands (10) vanished due to h-BN, as shown in Fig. 2(c–e). Moreover, this might be due to the suppression of vibrations of h-BN due to the accumulation of excess amount of h-BN. The excess quantity of h-BN (90 wt%) beyond a certain limit into ZrO_2 may restrict these particular usual vibrations. However, some peaks appeared in the wavenumber range from 586–590 cm^{-1}, 767–814 cm^{-1}, 1338–1383 cm^{-1}, and 2358 cm^{-1}, and confirmed the presence of ZrO_2.[65] Eventually, an absorption band (15) was observed in the wavenumber range from 3199–3451 cm^{-1} in all the IR spectra of the nanocomposite samples, which was accredited to O–H stretching.

Table 3 Density, percentage of porosity and mechanical properties of different bone implant materials

Bone implant materials	Density ($g\ cm^{-3}$)	Porosity [%]	Compressive strength [MPa]	Young's modulus [MPa]	References
Titanium (porous)	4.5	48	54 ± 5	7.7 ± 2	61 and 73
HAp	2.1	41	34 ± 2	—	74
0.5 La_2O_3-HAp (solid state route)	2.85	9.66	108.89 ± 1	90.81 ± 0.5	75
50BN–50B_2O_3 (thin film)	1.3	~36.4	37 ± 5	—	16
Tricalcium phosphate	3.14	50	11 ± 1.3	—	76
3D graphene (SPS)	~1.42	42	40 ± 3	4.1 ± 0.5	77
hBN–ZrO_2 (solid state route)	2.54	~10	174 ± 1	9.84 ± 0.5	18
hBN–ZrO_2 (solid state route)	3.12	—	227 ± 1	10 ± 0.1 (GPa)	Current work
Pure ZrO_2 (sintered at 1000 °C for 3 h)	5.68	—	181 ± 1	9.053 ± 0.1	—

Table 4 Composite samples code, peak positions in Raman spectra of all the biocomposite samples

	Raman shift (cm^{-1})															
Samples code	1	2	3	4	5	6	7	8	9	10	11	12	13	14	15	16
10B90Z	103	179	191	221	307	333	346	382	475	501	537	558	615	638	—	—
20B80Z	103	179	191	223	308	334	346	384	475	505	537	557	621	639	—	—
60B40Z	103	179	191	223	307	332	349	381	475	—	—	—	616	638	881	1367
80B20Z	103	179	191	—	—	333	349	382	475	—	—	—	615	638	882	1367
90B10Z	104	179	191	—	—	333	349	385	475	—	—	—	616	638	882	1366

4.3. Raman spectroscopic analysis

Fig. S2(a and b)† represents the Raman spectra for (a) pure h-BN, (b) pure ZrO_2 whereas, Fig. S3(a–e)† depicts the Raman spectra for h-BN–ZrO_2 nanocomposites denoted as (a) 10B90Z, (b) 20B80Z, (c) 60B40Z, (d) 80B20Z, and (e) 90B10Z, respectively. The bands are represented by (1), (2), (3), (4), …(16) in the ascending order of the wavenumber of their appearance, similar to the IR results. The obtained Raman spectra of the composite samples yield a consistent peak at 1367 cm^{-1}, matching with the Raman peak of high quality crystalline h-BN, as shown in Fig. S3(a).†[66] Pure ZrO_2 exhibited its characteristic Raman active bands at various wavenumbers such as 45, 178, 189, 260, 330, 377, 476, and 642 cm^{-1}.[67–69] As h-BN was introduced into ZrO_2, few new bands at 882 cm^{-1} and 1367 cm^{-1} (already mentioned) appeared due to the characteristic bands of h-BN, some existing bands of ZrO_2 at 223, 307, 505, and 557 cm^{-1} disappeared dramatically and the remaining bands of ZrO_2 were shifted by the 0 to +5 cm^{-1} wavenumber and finally appeared at 179, 191, and 382 cm^{-1} in the spectra of all the composites.[70–73] Therefore, the typical bands of hBN–ZrO_2 nanocomposites were centred at 103, 333, 349, 476, 615, and 638 cm^{-1}. A strong reduction in the intensities of the characteristic bands of h-BN and ZrO_2 was observed on increasing the amount of h-BN from 20 wt% in ZrO_2. Thus, the results obtained from the Raman study are consistent with the IR results (Table 4).

4.4. X-ray photoelectron spectroscopic (XPS) analysis

The composition of the surface and chemical states of Zr, O, B, and N elements in the sample 10B90Z was further tested by using XPS technique. The XPS spectra are shown in Fig. 3(a–d), representing the existence of Zr, O, B, and N elements on the surface layer of the powder sample 10B90Z without any impurities. Moreover, Fig. 3 shows the observed binding energies corresponding to particular atomic states that constitute different elements that were recognized as 182.4 and 180.15 eV for Zr 3d, 528.4 eV for O 1s, 396.1 and 395.9 eV for N 1s, and 182.45 eV for B 1s.[16,74,75] Fig. 3(a) shows the high-resolution spectrum of Zr 3d, in which two peaks were observed at 180.15 eV (Zr $3d_{3/2}$) and 182.4 eV (Zr $3d_{5/2}$) with enough

Table 5 Assignments of infrared and Raman bands in the spectra of various composite samples, 10B90Z, 20B80Z, 60B40Z, 80B20Z, 90B10Z respectively

Wave number range (cm^{-1}), IR	Wave number range (cm^{-1}), Raman	IR assignments	Raman assignments
0–507 & 586–590	145, 178, 189, 260, 330, 377, 476, 642	Occurred due to ZrO_2	Characteristic Raman active bands of pure ZrO_2
643.28–646.18, 767–814.95, 876–883, 922–923, 1060–1072	882, 1367	h-BN vibrational modes[59]	Characteristic bands of h-BN
1193	—	Bending vibrational mode of B–O–H	—
1338–1386	1367	Stretching vibrations of B–N[60]	Raman peak of high quality crystalline h-BN[66]
1456–1517	—	Stretching vibrations of B–O	—
1386–1456	—	It produced that might be due to the nearly the same involvement of the intensities of vibrations of both h-BN and ZrO_2	—
1634–1627	—	Appeared due to ZrO_2	—
1627–1634, 2030–2032, 2257–2258, 2358 & 2515	—	Appeared owing to h-BN	—
586–590, 767–814, 1338–1383 & 2358	—	Confirmed the presence of ZrO_2 (ref. 61)	—
3199–3451	—	Stretching vibration of O–H group of atmospheric moisture	—

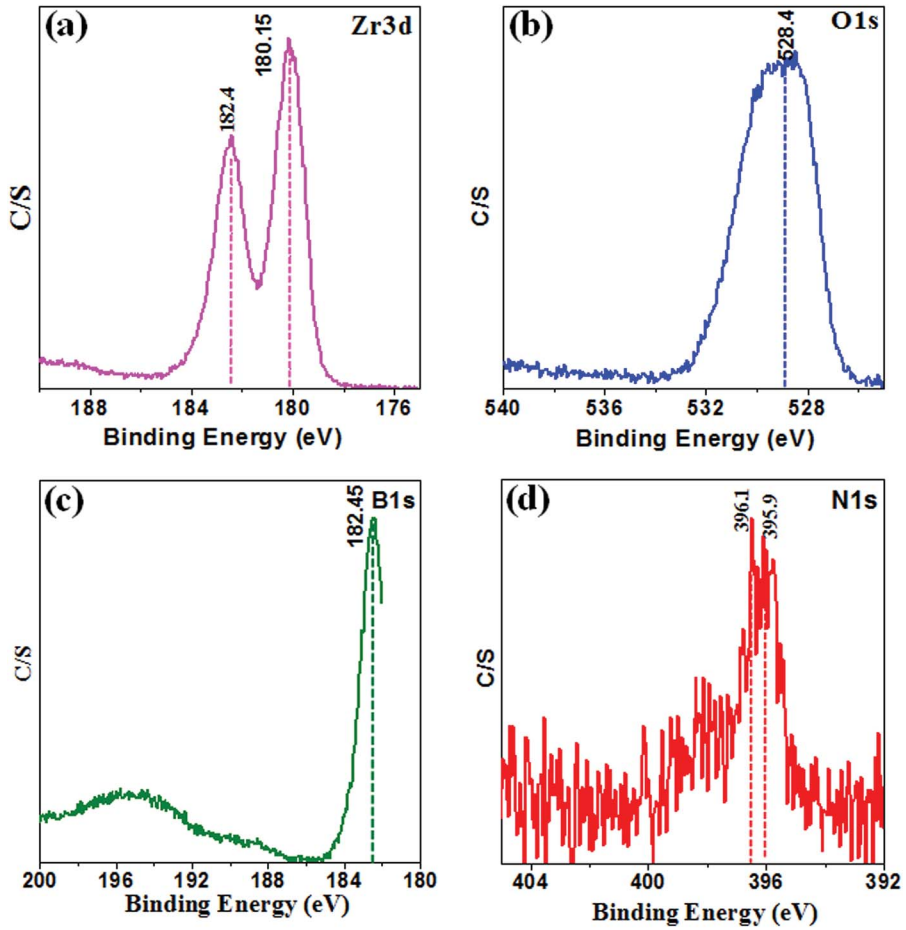

Fig. 3 XPS spectra of the 10B90Z composite samples sintered at 1200 °C showing four different peaks (a) Zr 3d reveals a typical ZrO_2 formation and shows two separate peaks at binding energies of 182.4 eV and 180.15 eV. (b) O 1s spectra show the main binding energies of oxygen at 528.4 eV. (c and d) Showing different peaks of B and N designated as core level B 1s and core level N 1s with the main binding energies of 182.45 eV, 395.9 eV, and 396.1 eV, respectively.

separation of 2.25 eV. However, Fig. 3(b and c) depicts the spectra of O 1s and B 1s, in which a single peak in each spectrum was observed at 528.4 eV and 182.45 eV that implies the formation of B–O and B–N bonding.[76,77] The N 1s peaks of the particular XPS spectrum revealed two different peaks of nitrogen at 396.1 eV and 395.9 eV, which could be the binding energy of B–O and B–N (Fig. 3(d)).[14] Therefore, the B 1s binding energy in B–(O, N) atmosphere is superior than that in B–O atmosphere, where the N atom replaces the O atom.

4.5. BET analysis

In this study, the surface area and average pore size of few selected nanocomposites 10B90Z, 60B40Z, and 90B10Z were measured with the help of nitrogen (N_2) adsorption/desorption isotherms using BET analyzer (Fig. 4(a–d)). These nanocomposites exhibit plentiful microporous channels (2 nm < width). The adsorbed content of N_2 with respect to relative pressure, P/P_0 was found to be maximum in the range of 0.4 to 0.9 and showed a high-quality hysteresis loop (Fig. 4(a and b)). The usual pore size distributions and surface area of the composite samples are shown in Fig. 4(c and d). It is clearly noticed that with increasing the weight% of h-BN, the average pore size and specific surface area of the nanocomposite samples 10B90Z, 60B40Z, and 90B10Z also increased from 1.21 nm to 1.66 nm and 21.011 $m^2\ g^{-1}$ to 65.66 $m^2\ g^{-1}$, respectively. It is noticed that sample 90B10Z has the highest surface area of around 65.666 $m^2\ g^{-1}$ but has an average pore size of 1.66 nm, whereas the sample 60B40Z has a surface area of about 31.07 $m^2\ g^{-1}$ but it has an average pore size of 1.64 nm. Even though the average pore size is more in sample 90B10Z than sample 60B40Z, the number of pores present in sample 90B10Z or the porosity of it is more than that of sample 60B40Z and hence, sample 90B10Z has more surface area. h-BN has a highly porous nature so the pore size and surface area both increase with increasing amount of BN. Fig. 4(d) depicts that the synthesized composites can have high BET specific surface area. Therefore, large surface area and established microporous architecture can play a pivotal role in cell growth. Fig. 8(d and e) represents the comparison of the surface area as well as average pore size for the individual nanocomposite samples.

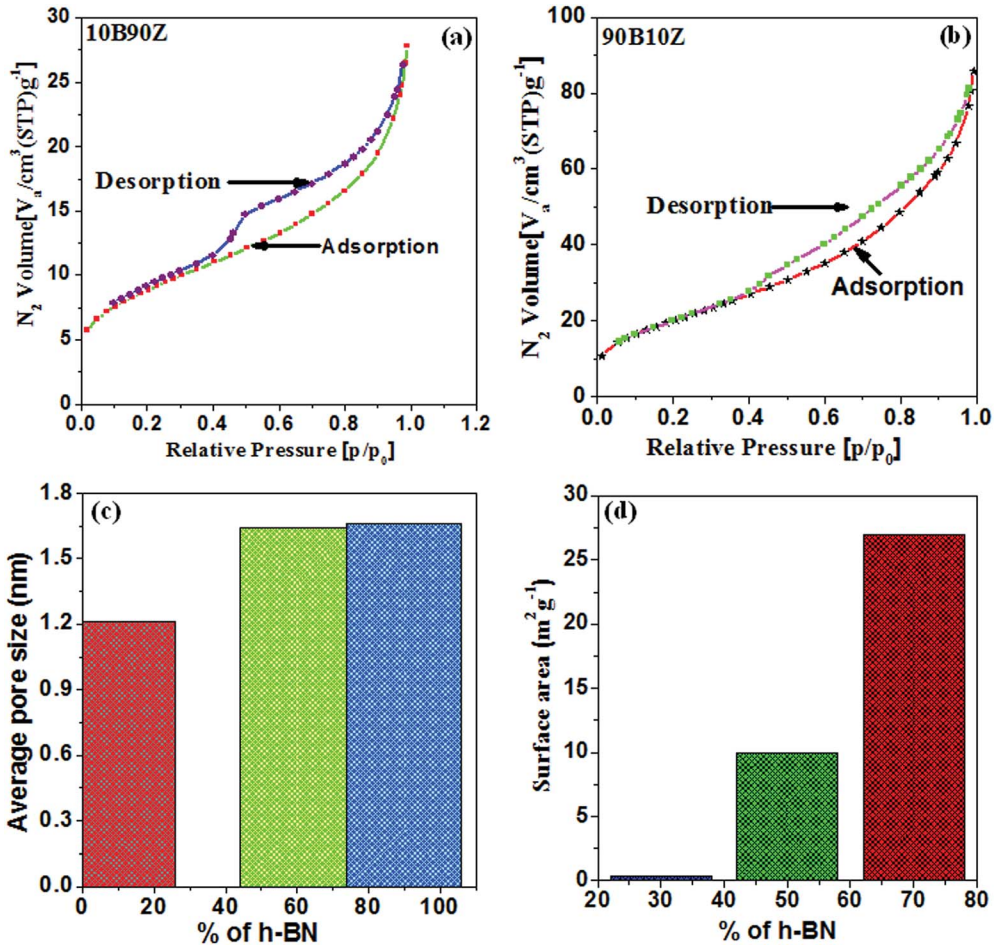

Fig. 4 Nitrogen adsorption–desorption curves for composites (a) 10B90Z and (b) 90B10Z sintered at 1200 °C for 3 h, (c) bar diagram for average pore size *vs.* increasing percentage of h-BN, and (d) bar diagram for surface area *vs.* increasing percentage of h-BN.

4.6. Scanning electron microscopic (SEM) analysis

The morphological features of the nanocomposites were studied using SEM. Fig. 5(a–e) depicts the SEM images of few selected samples (a) 10B90Z, (b) 20B80Z, (c) 40B60Z, (d) 60B40Z, and (e) 90B10Z, respectively. The interrelated grains and their boundaries were observed that gave rise to the crystalline nature of the prepared materials. The fine grains of ZrO_2 and h-BN sheets are represented by yellow and light green coloured arrows, respectively. The SEM images of the composite 10B90Z (Fig. 5(a)) divulged the development of small grains of ZrO_2 dispersed in the large, interconnected, and stacked h-BN sheets and 20B80Z showed mixed and uniform grains of h-BN and ZrO_2 (Fig. 5(b)). However, the image Fig. 5(c) for 40B60Z clearly depicts the porous and layered structure of h-BN with ZrO_2 grains. The images Fig. 5(d and e) for the samples 60B40Z and 90B10Z showed fully developed and randomly oriented h-BN nanosheets of thickness ~100–200 nm and side ~0.5–2 μm. The ZrO_2 nanoparticles were hardly seen due to two main factors: one is that the weight percentage of h-BN is larger than that of the ZrO_2 and the second one is that the density of h-BN (2.1 g cm^{-3}) is comparatively lesser than that of ZrO_2 (5.68 g cm^{-3}), so h-BN nanosheets covered most of the volume in the samples 60B40Z and 90B10Z. Moreover, the substitution of h-BN into ZrO_2 reduced the brittleness of ZrO_2 and induced ductility in the sample that agreed with the stress–strain results (Fig. 7(b)). The composition obtained by addition of a suitable amount of h-BN into ZrO_2 was strongly expected to be analogous to the natural bone composites. The nanocomposite sample 10B90Z withstands a maximum load of up to 227.33 MPa. It is accomplished from the SEM results that the reinforcement of h-BN into ZrO_2 amazingly improved the stability of the ZrO_2 with remarkable enhancement in the surface properties.

4.7. Transmission electron microscopic (TEM) analysis

Apart from the surface morphological studies, the TEM study was also carried out to analyse the more magnified view of the nanocomposite 10B90Z at the nanoscale level (Fig. 6(a–f)). Similar to SEM investigations, the mixed h-BN nanosheets and ZrO_2 nanoparticles are clearly observed in the TEM images also. In the images, the red coloured arrows indicate the laterally oriented h-BN nanosheets whereas the white coloured arrows show the presence of ZrO_2 nanoparticles. The

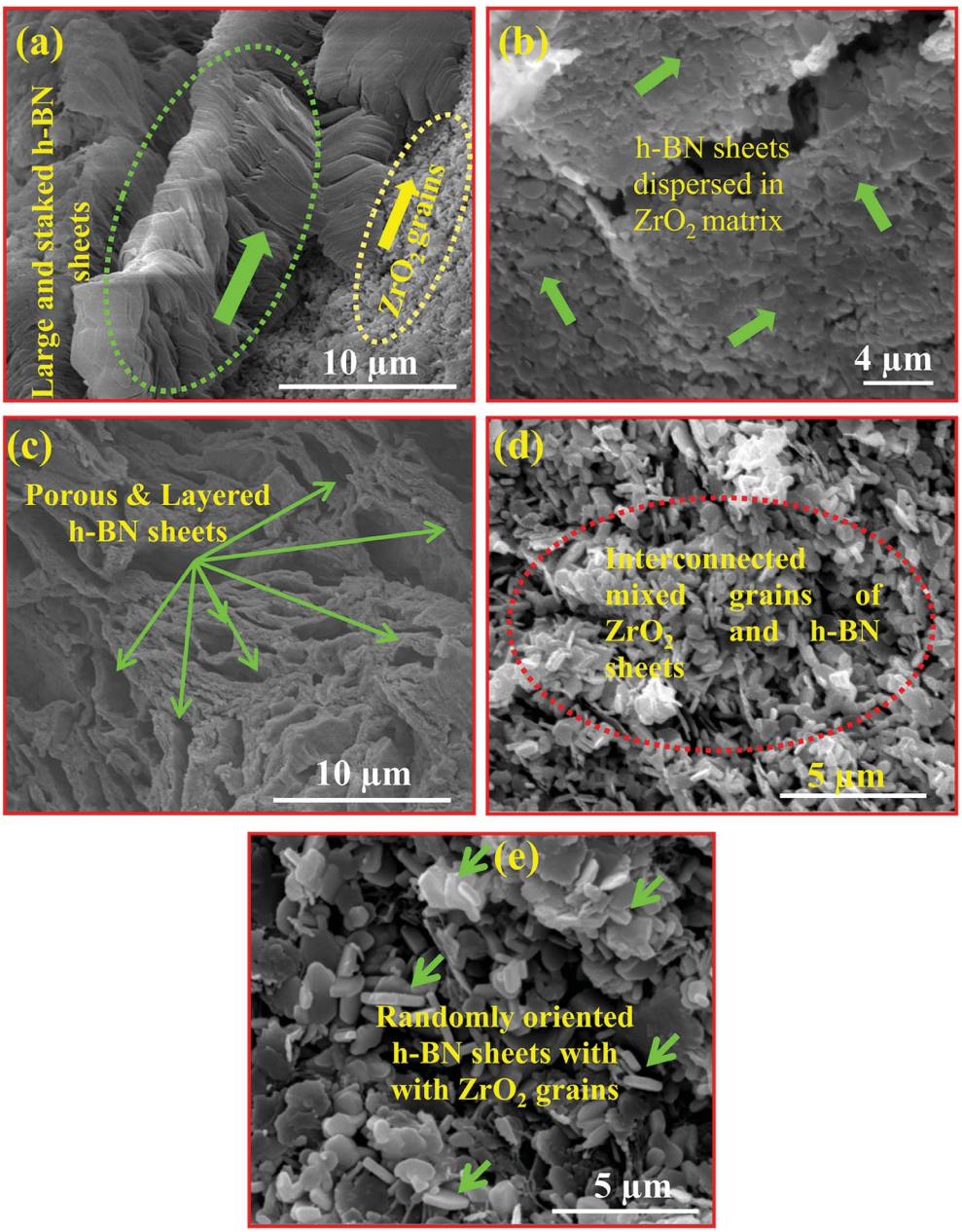

Fig. 5 Scanning electron micrographs of polished composites (a) 10B90Z, (b) 20B80Z, (c) 40B60Z, (d) 60B40Z, and (e) 90B10Z sintered at 1000 °C for 3 h.

average particle size (side of h-BN) of the h-BN nanosheets was found to be in the range of 500–1000 nm, which again has a good agreement with the SEM results. However, the particle size of nano ZrO_2 was found to be in the range of 5–10 nm. The fine ZrO_2 nanoparticles are well dispersed with large h-BN nanosheets and appeared darker than individual h-BN nanosheets. The high resolution (HR-TEM) image (Fig. 6(e)) exhibited the symmetrically arranged layered structure of h-BN nanosheets separated by a distance of 76 nm. The SAED pattern showed various diffraction rings associated with various lattice planes (000), (002), (101), (004), and (110) of h-BN (Fig. 6(f)).[18]

4.8. Density analysis

The densities of all the sintered pellets were determined from the geometrical dimensions and their respective masses. Fig. 7(a) shows the density values of the prepared nanocomposites of h-BN–ZrO_2. It is obvious from Fig. 7(a) that the density decreases with successive increments in the amount of h-BN or decrease in the amount of ZrO_2 due to the inferior density of h-BN (2.1 g cm^{-3}) in comparison to the density of pure ZrO_2 (5.68 g cm^{-3}). Moreover, the determined values of density vary from 2.67 g cm^{-3} to 3.12 g cm^{-3} for all composites, *viz.*, 3.12, 3.04, 2.82, 2.79, 2.70, and 2.67 g cm^{-3} for 10B90Z, 20B80Z, 40B60Z, 60B40Z, 80B20Z, and 90B10Z, respectively (Table 1).

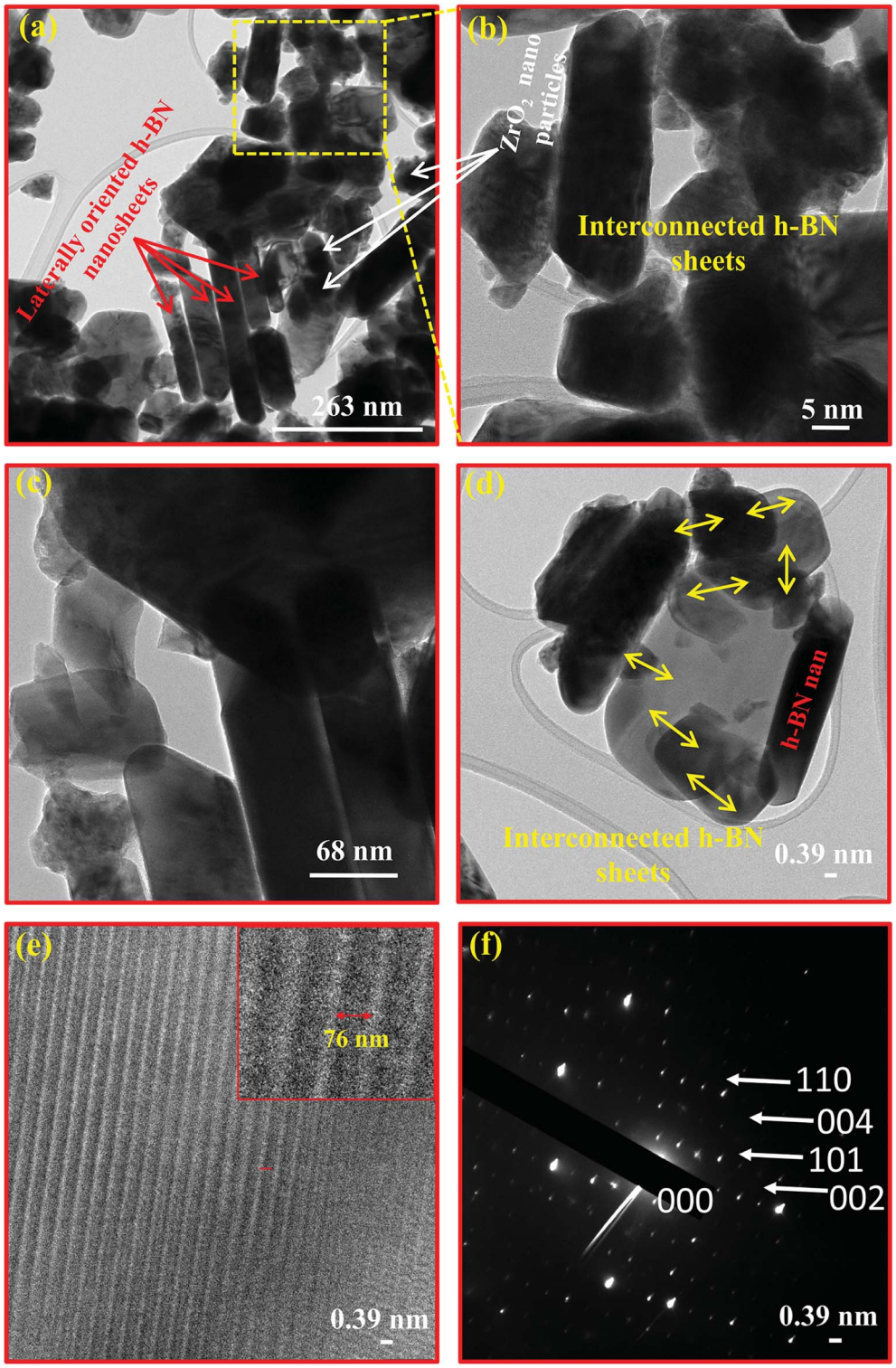

Fig. 6 Transmission electron microscopy of the nanostructured composite sample 10B90Z (a) low magnification TEM image showing ZrO_2 nanoparticles embedded in h-BN sheets. (b and c) High magnification TEM images showing interconnected large nanorods of hBN–ZrO_2 nanoparticles. (d) High magnification bright field TEM image showing interconnected large h-BN sheets consisting of ZrO_2 nanoparticles. (e) High resolution TEM image clearly showing the very fine arrangement of large nanorods. (f) Selected area electron diffraction pattern (SAED) showing spotty (ZrO_2) and crystalline pattern of h-BN.

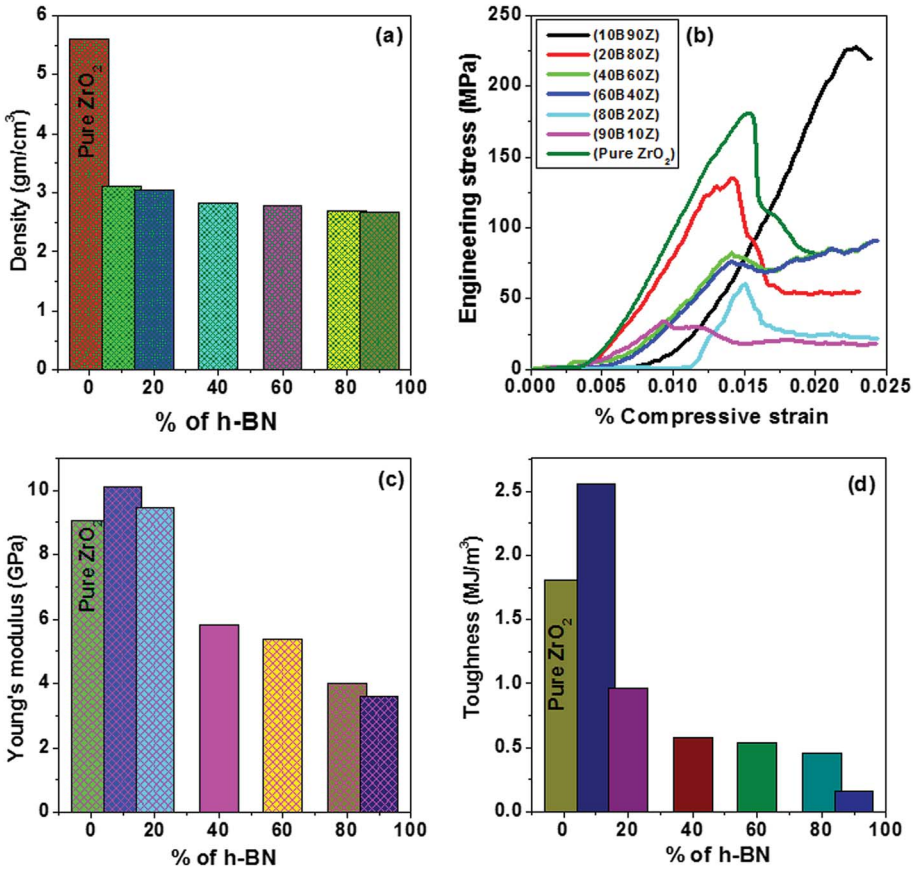

Fig. 7 (a) Density of pure ZrO_2 and hBN–ZrO_2 biocomposite samples with variation of h-BN. (b) Engineering stress *vs.* % of compressive strain graph of pure ZrO_2 and hBN–ZrO_2 samples sintered at 1000 °C for 3 h. (c) Variation of Young's modulus of pure ZrO_2 and hBN–ZrO_2 samples with varying concentration of h-BN. (d) Dependency of toughness of pure ZrO_2 and hBN–ZrO_2 composite samples with variation of h-BN.

4.9. Mechanical behaviour

The stress–strain graphs for pure ZrO_2, 10B90Z, 20B80Z, 40B60Z, 60B40Z, 80B20Z, and 90B10Z nanocomposites are given in Fig. 7(b). It is noticed from Fig. 7(b) that on increasing the amount of h-BN into ZrO_2, the mechanical strength, Young's modulus, and toughness decrease (Table 1). Moreover, due to less density of h-BN and its highly lubricating nature, it provides the flexibility to the synthesized composites that inhibit the brittleness of the composites. However, the nanocomposite 10B90Z achieved the highest compressive strength of ~227 MPa along with adequate values of Young's modulus and fracture toughness 10.10 GPa and 2.56 MJ m^{-3}, respectively. This composite also has a density of 3.12 g cm^{-3}, which is very close to that of natural teeth.[78] It is well known that ZrO_2 has superior mechanical properties due to its dense microstructure. When ZrO_2 is added with h-BN and sintered at 1000 °C, they are strongly bonded with each other and provide better strength to the final product. The fine spherical particles linked on the h-BN surface are mostly the minor phase of ZrB_2 and ZrB. Because these two kinds of particles have enormous modulus and mechanical strength, they contribute to the reinforcement of the hBN–ZrO_2 composites.[79] Moreover, the typical SEM image (Fig. 5(a)) of this composite sample shows a unique morphology, *i.e.*, the formation of stacked h-BN grains during the sintering process. When the compressive load is applied, the stacked h-BN grains prevent the crack propagation and hence, the composite shows its maximum strength. Thus, these findings fulfilled the mechanical criteria for this nanocomposite as a capable alternative to artificial teeth and dental implants. The hBN–ZrO_2 composites expressed trivial deformability, which occurs due to the ductile nature of h-BN that prevents disastrous failures.[18] Thus, the addition of h-BN into ZrO_2 paves the way to reduce the brittle nature of pure ZrO_2 that could stand better than natural bone. The Young's modulus and toughness decreased with increasing concentration of h-BN in ZrO_2 (Fig. 7(c–d)). The comparative analysis of density, porosity, Young's modulus, and compressive strength of the various composite samples obtained *via* different synthetic routes, as reported in the literature, with the synthesized composite sample 10B90Z is given in Table 3 along with suitable references. Among all the synthesized nanocomposite composites, 10B90Z was found to be the best and superior in comparison to the reported biomaterials such as porous titanium (pTi), nHAp, La_2O_3-Hap, tricalcium phosphate, and 3D graphene.[80–84]

4.10. Tribological analysis of the composite samples

The tribological characteristics of the few selected samples 10B90Z, 60B40Z, and 90B10Z sintered at 1000 °C for 3 h were

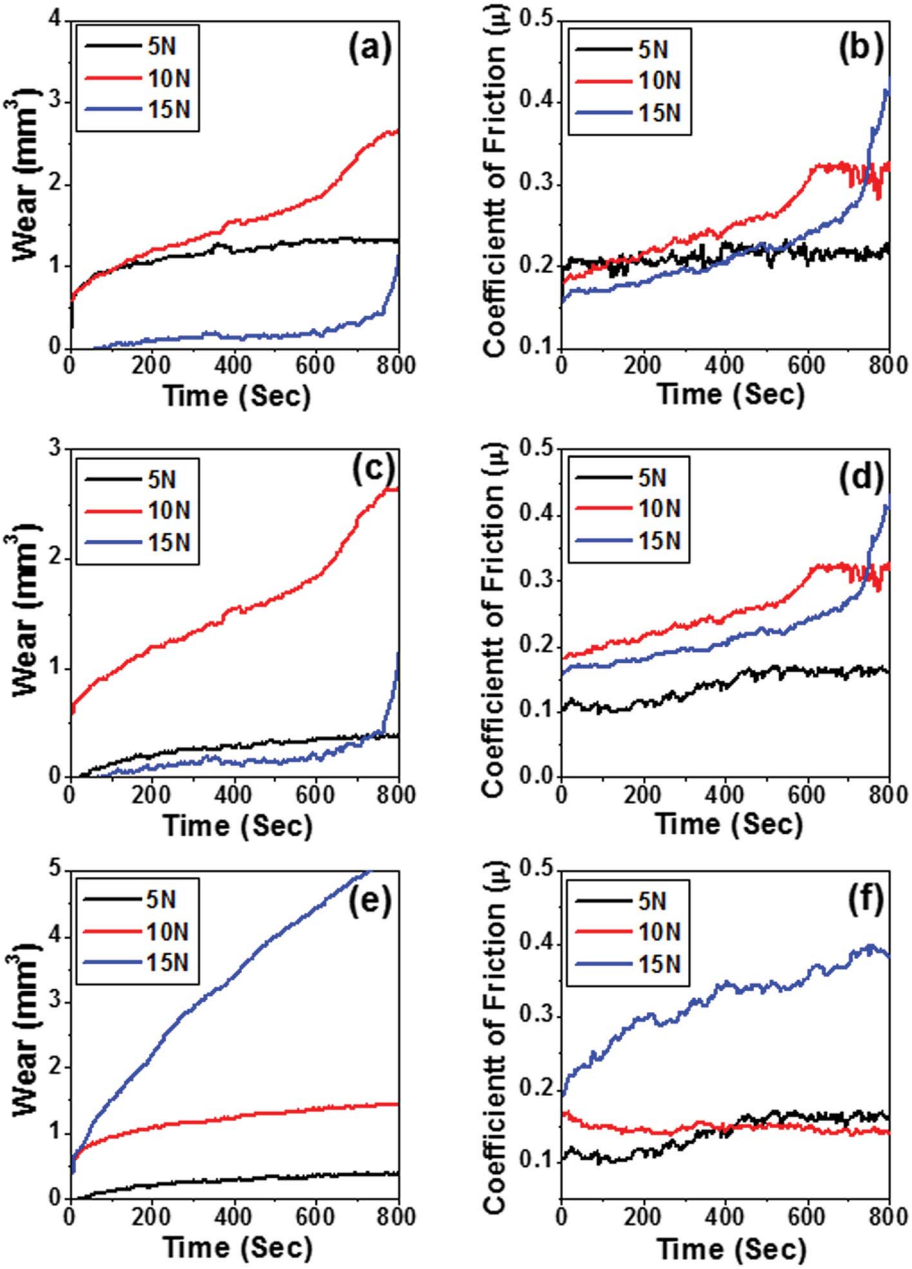

Fig. 8 Variations of wear against sliding time and coefficient of friction against sliding time at different loads of the composite samples (a and b) 10B90Z, (c and d) 60B40Z, and (e and f) 90B10Z sintered at 1000 °C for 3 h.

tested to analyze their wear and coefficient of friction behaviors. Fig. 8(a–e) shows the variation of wear and coefficient of frictional force with sliding time for the above composite samples. The weight loss of the materials at 15 N load is found to be significantly lesser than that at 5 N and 10 N loads, whereas weight loss is maximum for 10 N load (Fig. 8(a–c)). Fig. 8(e) reveals the higher weight loss at load 15 N and minimum at load 5 N. As the concentration of h-BN increases and the percentage of ZrO_2 decreases at higher load (15 N), the weight loss increases appreciably. However, in all the above mentioned nanocomposites, a moderate wear property was observed for 5 N loads. Thus, these composites may be recommended for wear resistance materials for low loads. It is noticed that the variation of coefficient of friction for all the compositions is fluctuating in nature and within the range of 0.1 to 0.4 (Fig. 8(b, d and f)). In the present investigations, at higher load, the coefficient of friction is higher than that at a lower load of 5 N. Therefore, the optimum value of all compositions occurs at 5 N load. Eventually, the present developed nanocomposite is suitable for 5 N load. On increasing the reinforcement of h-BN in ZrO_2, the composite becomes ductile in nature, and owing to the ductile and soft nature of h-BN, the sufficient weight loss was found to increase beyond a certain limit of h-BN concentration. Therefore, in view of the tribological properties, the composite

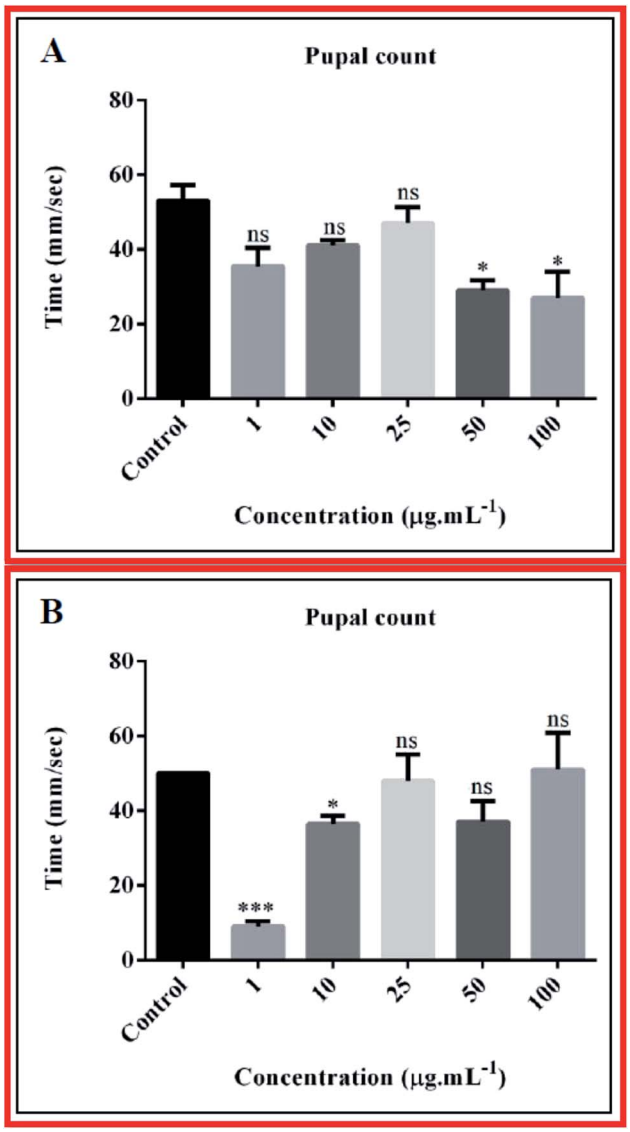

Fig. 9 Pupal count of fly. (A) Pupal count of composite 10B90Z, showing no significant changes in all the concentrations while the higher concentrations show a slight decrease in the pupal count. (B) Pupal count of composite 90B10Z, showing a decrease in the pupal count at lower concentrations while it was unaffected at higher concentrations. *** designates $p < 0.001$ and * designates $p < 0.05$.

10B90Z sample was found to be very compatible with teeth implant applications.

5. Biological activities

5.1. Life cycle analysis

Nanocomposites may induce defects in the developmental cycle of the fly. But in our case, we did not observe any delay in developmental cycle. From pupal count of third day after appearance of pupa, we observed that the composite 10B90Z (Fig. 9(A)) induced a negative impact on the pupal number at high concentration (100 μg mL^{-1}) with the value 19.50 ± 2.500, which is less than that of the control (51.00 ± 5.000). However, at lower concentrations such as 1 μg mL^{-1}, 10 μg mL^{-1}, 25 μg mL^{-1}, and 50 μg mL^{-1}, no such significant changes were observed and the values were 36.00 ± 4.000, 37.00 ± 5.000, 40.00 ± 4.000, and 29.00 ± 2.000, respectively. The composite 10B90Z, in most of the cases, has no impact on the pupal count. From the pupal count of the third day after appearance of pupa, we observed that the composite 90B10Z (Fig. 9(B)) induced negative impact on the pupal number count in lower concentrations such as 1 μg mL^{-1} and 10 μg mL^{-1}, whose values were 9.000 ± 1.000 and 36.50 ± 1.500, respectively. However, at higher concentrations such as 25 μg mL^{-1}, 50 μg mL^{-1}, and 100 μg mL^{-1}, no such significant changes were observed, which was confirmed by the values 48.00 ± 5.000, 37.00 ± 4.000, and 51.00 ± 7.000, respectively. The control value for pupal count was 50.00 ± 0.0. This result suggests that nanocomposite 90B10Z induces damage to pupal development at lower concentrations. However, the nanocomposite 10B90Z has no impact on the pupal count, which revealed the superiority of 10B90Z over 90B10Z.

5.2. Larva crawling assay

The larva crawling assay was done to check any neuronal defects in the larva due to ingestion of nanocomposites 10B90Z and 90B10Z through food. The wild type larvae or the control ones moved almost in a straight line from the centre of the petri dish towards the periphery, whilst many treated larvae traveled confused and curvy paths, and some traveled almost negligible distances. The larvae treated with different concentrations of the sample 10B90Z also showed some confused movements in the crawling plates, which can be observed from the traced path (Fig. 10(A)). At concentrations such as 1 μg mL^{-1}, 50 μg mL^{-1}, and 100 μg mL^{-1}, the path traveled by the larvae is not straight and was confusing. Some larvae took a lot more time to reach the periphery as compared to the control larvae. More than half of the larvae treated with the highest concentration of 10B90Z, *i.e.*, 100 μg mL^{-1}, didn't travel a significant path. This suggests neuronal damage of the larvae. Mostly, the damage of the larvae is seen at higher concentrations.

In Fig. 10(B), we can see that the path traced by the larvae treated with 10 μg mL^{-1} was very curvy and it fails to reach the periphery. Also, for those treated with 25 μg mL^{-1} concentration, the path travelled to reach their destination was very long and curvy, which shows confused behaviour of the larvae. This suggests that some motor neurons of the larvae were affected by the nanocomposite 90B10Z at lower concentrations.[85] This data shows similarity with literatures where nanoparticles induced toxicity affects the neuronal health of the fly.[86,87] To validate the crawling assay, we checked the speed of the larva treated with nanocomposite 10B90Z. In Fig. 10(C), the control crawling speed was found to be 1.544 ± 0.1075. We did not find any significant changes in the speed at 10 μg mL^{-1} and 25 μg mL^{-1} treated larvae, whose speeds were found to be 1.206 ± 0.1181 and 1.310 ± 0.1089, respectively. On the other hand, in the case of 1 μg mL^{-1}, 50

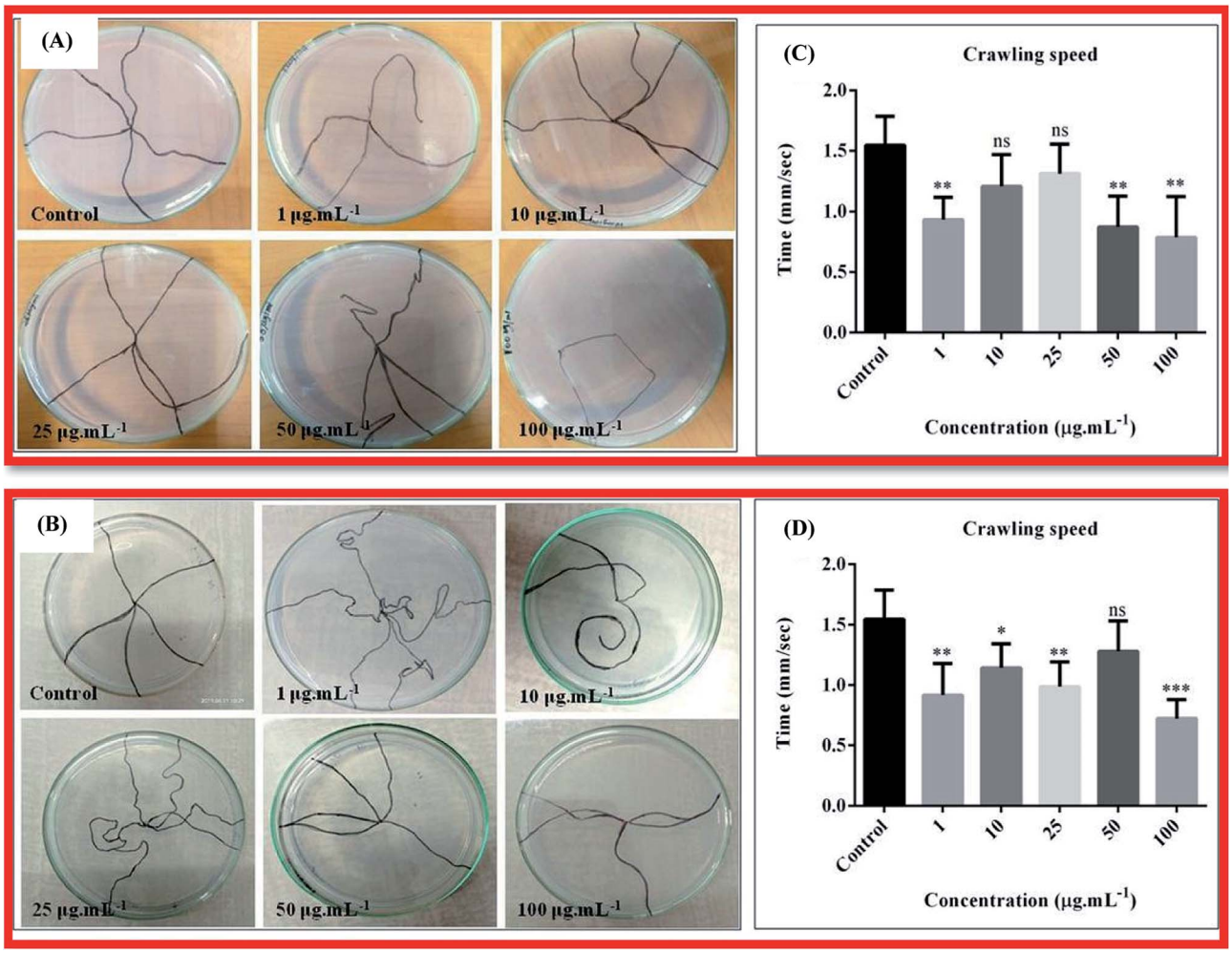

Fig. 10 Crawling assay of the third instar larvae. (A) Crawling behavior of composite 10B90Z treated larvae. Some paths are incomplete as they did not reach the periphery due to slow movement. (B) Crawling behavior of composite 90B10Z treated larvae. As shown in the figure, at lower concentrations, complex tracking paths were observed with a number of twist and turns unlike that of the controls. Mostly, at higher concentrations, a complex pathway of crawling was seen. (C) Speed of the larvae of composite 10B90Z. (D) Speed of the larvae of composite 90B10Z (in each case, $N = 6$). *** designates $p < 0.001$, ** designates $p < 0.01$, and * designates $p < 0.05$.

μg mL^{-1}, and 100 μg mL^{-1}, the values were 0.9320 ± 0.08194, 0.8720 ± 0.1127, and 0.7860 ± 0.1498, respectively, which show a significant decrease in the crawling speed, thus indicating the defective pattern of crawling.

Therefore, to validate the crawling assay, we also checked the speed of the larva treated with nanocomposite 90B10Z (Fig. 10(D)). The control crawling speed was found to be 1.494 ± 0.08886. We did not find any significant changes in the speed of 50 μg mL^{-1}; the value was 1.280 ± 0.1121 mm s^{-1}. 1 μg mL^{-1}, 10 μg mL^{-1}, 25 μg mL^{-1}, and 100 μg mL^{-1} showed a decrease in the crawling speed, which was found to be 0.9500 ± 0.1095, 1.142 ± 0.08930, 0.9856 ± 0.09226, and 0.7200 ± 0.07092 mm s^{-1}, respectively.

5.3. Trypan blue staining

In order to check the dead cells inside the gut of the larvae, trypan blue test was also performed. It differentiates the dead cells from the live cells by staining the dead cells blue while the live cells are unaffected. In Fig. 11(A), only mild gut damage was seen in the third instar larvae at 100 μg mL^{-1} concentration of the nanocomposite 10B90Z. All the larvae from other treated concentrations of the nanocomposite 10B90Z gave negative results to the trypan blue test. This suggests that this has no toxic effect on the gut of larva.

Fig. 11(B) suggests gut damage at lower concentrations such as 1 μg mL^{-1}, 10 μg mL^{-1}, and 25 μg mL^{-1} while the larva with high concentrations shows a negative result to the test. This may be due to agglomeration of nanoparticles at higher concentrations. Mild damage in the gut was seen at 1 μg mL^{-1} concentration larva while severe gut damage was seen in the third instar larvae of 10 μg mL^{-1} and 25 μg mL^{-1} concentrations of the nanocomposite 90B10Z. From this result we can confirm that the nanocomposite 90B10Z causes damage to the gut tissues when employed at lower concentration.

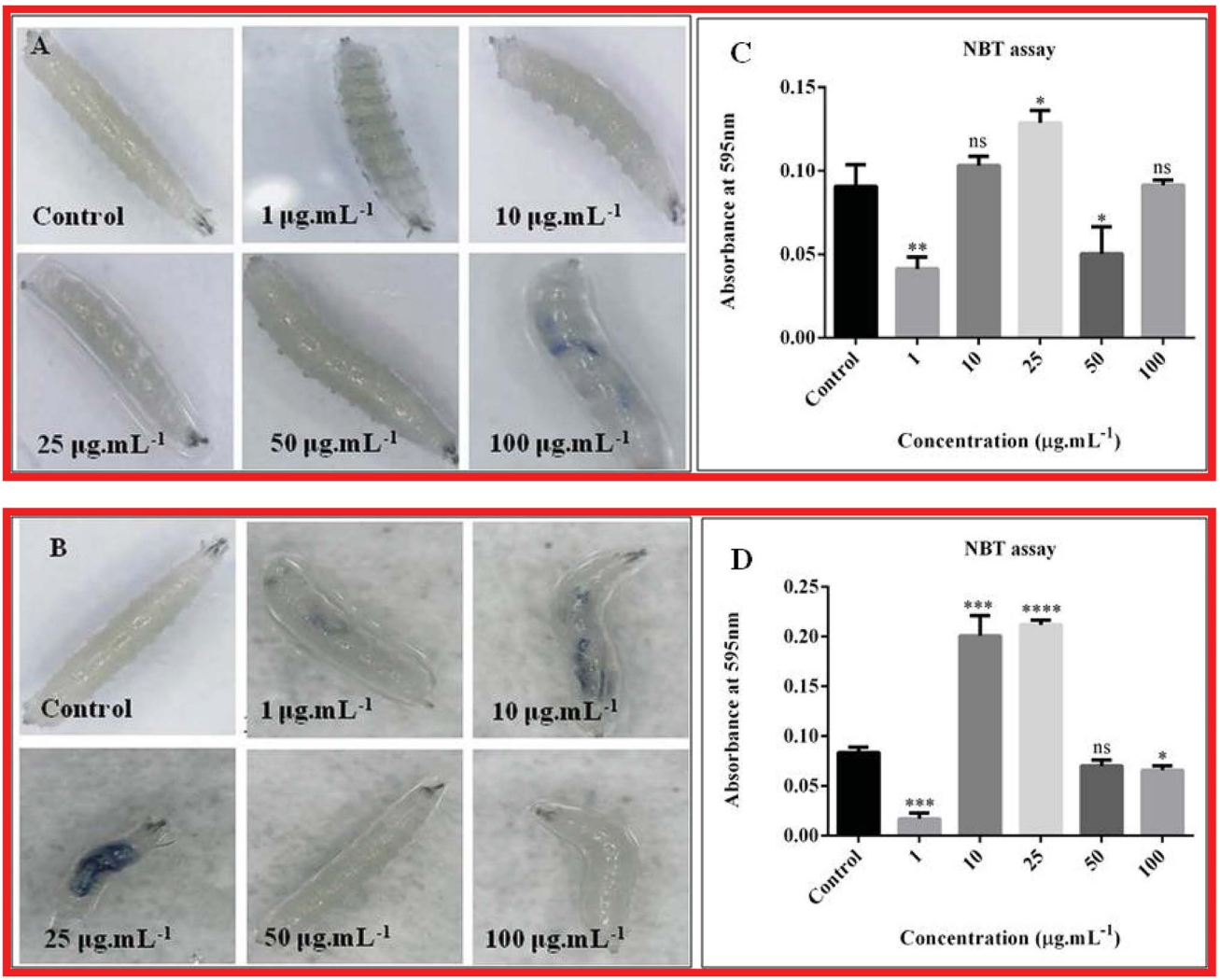

Fig. 11 (A) Trypan blue staining of the composite 10B90Z. At higher concentrations, a blue color stained gut was observed ($N = 6$). (B) Trypan blue staining of composite 90B10Z. Blue color in the larva indicating damaged portions of the gut at lower concentrations. (C) NBT assay of composite 10B90Z. In most of the cases, ROS production is less or equal to the control. (D) NBT assay of 90B10Z. Lower concentrations showing more absorbance indicate more ROS production. Only at a moderate concentration, more ROS production is observed ($N = 15$). **** designates $p < 0.0001$, *** designates $p < 0.001$, ** designates $p < 0.01$, and * designates $p < 0.05$.

5.4. NBT reduction assay for ROS production

The verification of quantity of ROS generated in the haemolymph of third instar larvae after up taking nanoparticles was done through NBT assay. The amount of ROS generation is directly proportional to the absorbance. For nanocomposite 10B90Z, (Fig. 11(C)) absorbance for ROS of control was found to be 0.09067 ± 0.007535. At 1 μg mL^{-1} and 50 μg mL^{-1}, the value was decreased to 0.04133 ± 0.004096 and 0.05033 ± 0.009333, respectively, showing no increase in ROS generation. Also, we did not find a significant change in the absorbance at 10 μg mL^{-1} and 100 μg mL^{-1}, which was 0.1030 ± 0.003215 and 0.09133 ± 0.001764, respectively, which is equivalent to the control showing no increase in ROS generation but a significant increase was observed in 25 μg mL^{-1}, which was 0.1287 ± 0.004256. In each case, the experiment was repeated three times. Herein, most of the concentrations show negative effect to increased ROS generation. Only at 25 μg mL^{-1} toxicity was seen. Hence, we can infer that this nanoparticle is less toxic when applied in all these concentrations.

For the nanocomposite 90B10Z, (Fig. 11(D)) the absorbance for ROS of the control was found to be 0.08333 ± 0.003333. At 1 μg mL^{-1} and 100 μg mL^{-1}, the absorbance was found to be 0.0170 ± 0.003215 and 0.06567 ± 0.002667, respectively, which was less than that of the control, while no such significant changes were observed in the case of 50 μg mL^{-1}, which was 0.0700 ± 0.003464. Interestingly, at concentrations of 10 μg mL^{-1} and 25 μg mL^{-1}, a large increase in the ROS production was observed and the values were 0.2007 ± 0.01170 and 0.2117 ± 0.002848, respectively. The literatures suggest that the nanoparticles induce stress in the fly, resulting in oxidative damage.[88] So, ROS production will be more.[89] Lower concentrations of the nanocomposite 90B10Z were mostly affected by the nanoparticles. At higher concentration, the nanoparticle

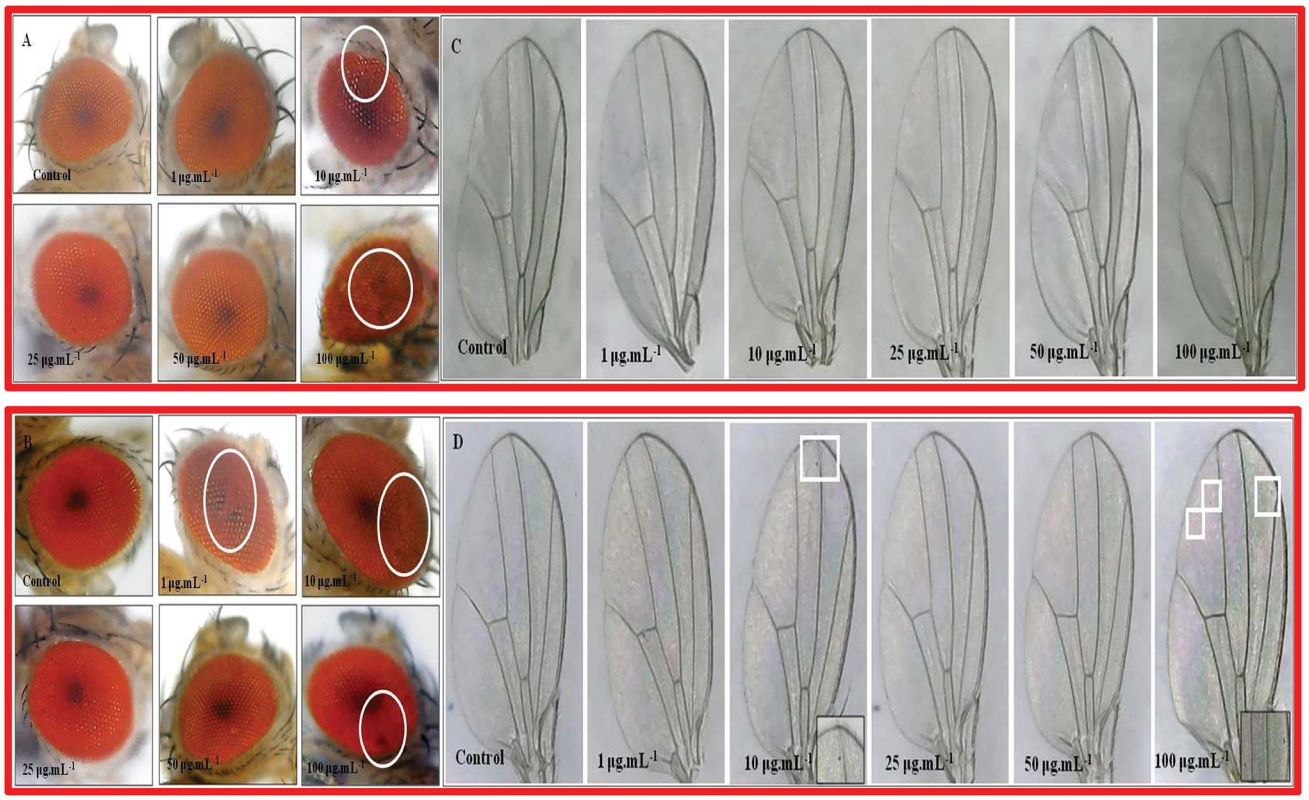

Fig. 12 (A) Adult eye phenotype of the composite 10B90Z. There is a loss of ommatidia found at the border of the eye at moderate concentrations shown in white circles, while at higher concentrations, a damaged eye can be seen ($N = 30$). (B) Adult eye phenotype of the composite 90B10Z. There are fused ommatidia structures observed in the eyes, indicated with white circles, whereas there is an ommatidia loss visible at 10 μg mL^{-1} and 50 μg mL^{-1} concentrations (marked with circles). (C) Adult wing phenotype of the composite 10B90Z showing no defects ($N = 30$). (D) Adult wing phenotype of the composite 90B10Z. The wings taken from the flies at different concentrations of the composite are compared against the control flies. A single spot was observed at 10 μg mL^{-1} and more spots were observed at 100 μg mL^{-1} concentration, marked with white rectangles.

size may become larger by agglomeration, so they cannot travel through all the tissues. This may be one of the reasons of less toxicity at higher concentration of the nanoparticles.

6. Adult phenotype assay

6.1. Eye phenotype

In nanocomposite 10B90Z (Fig. 12(A)), we found that at 10 μg mL^{-1} and 100 μg mL^{-1} concentrations, the structural arrangement of the eyes got disturbed. Ommatidial loss near the periphery region indicates the apoptosis of structures. At other concentrations, the eye structures were unaffected. In case of the composite sample 90B10Z (Fig. 12(B)) at lower concentrations such as 1 μg mL^{-1} and 10 μg mL^{-1}, we observed some ommatidia loss in the compound eye of *Drosophila*. The similar kind of eye defect was observed at higher concentrations. There were no such defects observed at 25 μg mL^{-1} and 50 μg mL^{-1} concentrations.

6.2. Wing phenotype

To check the toxic effect of the nanoparticles, the adult phenotypes were taken. For the nanocomposite 10B90Z (Fig. 12(C)), no such defects appeared in the adult. This suggests that the nanocomposite 10B90Z has no negative effect on wing development in the fly. For the nanocomposite 90B10Z (Fig. 12(D)), at 10 μg mL^{-1} as well as 100 μg mL^{-1} concentration, some black spots in wings were seen that are absent in the control wings. Wing spots were observed in the wings due to genotoxicity of the nanoparticles on the fly's body. Some previous data suggest that the nanoparticles have genotoxic effects that may lead to wing spot formation.[87] Therefore, the nanocomposite 90B10Z affects the normal development of wings at lower concentrations as well as higher concentrations.

6.3. Bristle phenotype

The genes achaete–scute complex are responsible for the proper formation of microchaetes in fly.[90] In the case of nanocomposite 10B90Z (Fig. 13(A)), no major defects were observed. However, at 25 μg mL^{-1} concentration, some bristles were absent in the thorax regions. This indicates that the nanocomposite 10B90Z has no damaging effect on the bristle patterning in *Drosophila*. In the composite sample 90B10Z (Fig. 13(B)), at 1 μg mL^{-1} concentration, formation of extra bristle was seen. A number of missing bristles at their respective regions were observed at 10 μg mL^{-1}. Previous reports suggest that the damage in bristle

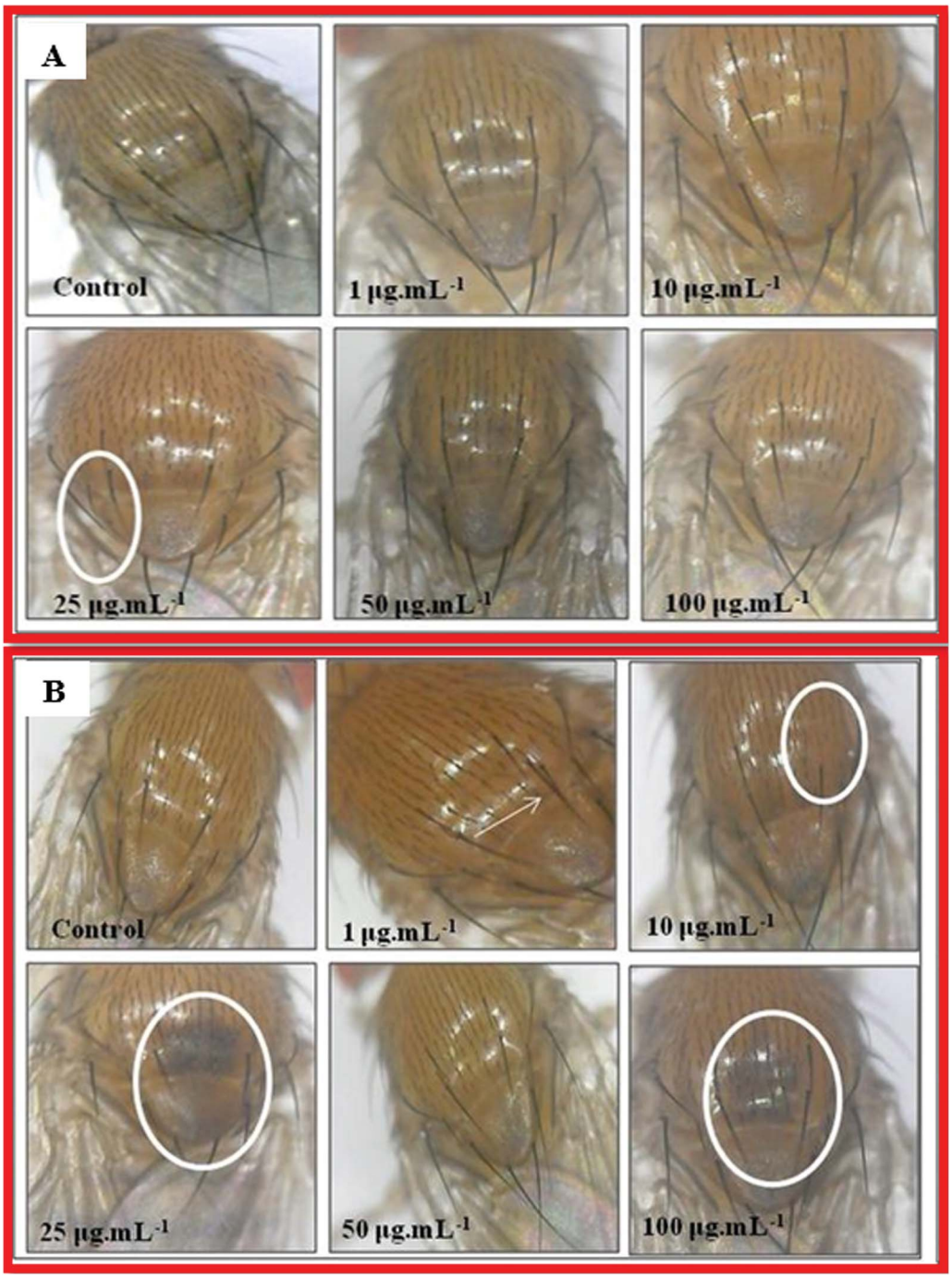

Fig. 13 (A) Adult bristle phenotype of the composite 10B90Z. No such major changes were observed. Only at a moderate concentration, a phenotype with missing bristle was found, which was marked with a white circle. (B) Adult bristle phenotype of the composite 90B10Z. At a lower concentration, extra bristle was formed indicated with white arrow, while in some cases, mechanization and loss of bristles were found, which are indicated with white circles ($N = 30$).

formation in *Drosophila* is due to nanoparticle uptake.[86,91] At 25 μg mL^{-1} and 100 μg mL^{-1} concentrations, the thorax region was melanized. The pigmentation in the thorax region of *Drosophila* is due to some genes such as *ebony* and *dopa*.[92,93] They are the key regulators of melanin synthesis in the fly's body.[94] Some previous studies on zirconia toxicity have shown the pigmentation at abdominal regions of the fly.[91] The defective patterning in pigmentation of the thorax of flies suggests that the nanocomposites affect the pigmentation genes only at higher concentrations.

7. Conclusions

The various 3-D nano biocomposites of hBN–ZrO_2 of high strength were successfully synthesized *via* solid state reaction method. Their structural, morphological, mechanical, and

tribological properties were well correlated. A fine interconnected network was observed in the microstructural study. The zirconia nanoparticles were finely decorated into large and organized hexagonal nanosheets of boron nitride. The nanocomposite 10B90Z showed less toxicity in the *in vivo* study using *Drosophila melanogaster*, while the composite 90B10Z showed toxicity in *Drosophila*. Due to the less toxicity of the composite 10B90Z, its utilization in nano formulation of various drug delivery systems can be proposed. Among all the synthesized compositions, the composite 10B90Z achieved the most significant mechanical, tribological, and biological properties compared to the desired properties for artificial teeth and teeth implant materials.

Conflicts of interest

The authors declare no competing financial interest.

Acknowledgements

C. R. G. appreciatively acknowledges the Science and Engineering Research Board, Department of Science and Technology (SERB-DST), New Delhi and Government of India for giving financial support under the Empowerment and Equity Opportunities for Excellence in Science (File No. EEO/2018/000647). A. G. acknowledges the University Grant Commission, Government of India, New Delhi for Junior Research Fellowship File No.: (Roll No. 525791 Sr. No. 2061451179 Ref. No: 22/06/2014 (i) EU-V). The authors also acknowledge the Centre of Excellence Scheme of U.P. State Government for providing PXRD facility at the Department of Physics, University of Lucknow. The authors also deeply acknowledge Prof. P. M. Ajayan, Department of Materials Science and Nano Engineering, Rice University, USA for providing the SEM/TEM and UTM facilities.

References

1 J. Eichler and C. Lesniak, *J. Eur. Ceram. Soc.*, 2008, **28**, 1105–1109.
2 C. Steinborn, M. Herrmann, U. Keitel, A. Schonecker, J. Rathel, D. Rafaja and J. Eichler, *J. Eur. Ceram. Soc.*, 2013, **33**, 1225–1235.
3 B. Ertug, T. Boyraz and O. Addemir, *Mater. Sci. Forum*, 2007, **554**, 197–200.
4 S. K. Lee, K. Nakamura, S. Kume and K. Watari, *Eco-Mater. Proc. Des. VII*, 2006, **510–511**, 398–401.
5 J. Eichler, K. Uibel and C. Lesniak, *Adv. Sci. Technol.*, 2010, **65**, 61–69.
6 A. Lipp, K. A. Schwetz and K. Hunold, *J. Eur. Ceram. Soc.*, 1989, **5**, 3–9.
7 W. S. Cho, M. W. Cho, J. H. Lee and Z. A. Munir, *Mater. Sci. Eng., A*, 2006, **418**, 61–67.
8 X. Duan, M. Wang, D. Jia, N. Jing, Z. Wu, Z. Yang, Z. Tian, S. Wang, P. He, Y. Wang and Y. Zhou, *Mater. Sci. Eng., A*, 2014, **607**, 38–43.
9 S. Guicciardi, R. Calzavarini, V. Medri, S. Bugliosi and A. Bellosi, *Mater. Sci. Eng., A*, 2007, **445–446**, 579–586.
10 H. Y. Jin, W. Wang, J. Q. Gao, G. J. Qiao and Z. H. Jin, *Key Eng. Mater.*, 2006, **317–318**, 637–640.
11 B. Lee, D. Lee, J. H. Lee, H. J. Ryu and S. H. Hong, *Sci. Rep.*, 2016, **6**, 1–12.
12 Y. L. Li, J. X. Zhang, G. J. Qiao and Z. Jin, *Mater. Sci. Eng., A*, 2005, **397**, 35–40.
13 S. A. Taylor and A. L. Moore, *J. Mater. Sci.*, 2015, **50**, 6220–6226.
14 S. Vinod, C. S. Tiwary, P. A. S. Autreto, J. T. Tijerina, S. Ozden, A. C. Chipara, R. Vajtai, D. S. Galvao, T. N. Narayanan and P. M. Ajayan, *Nat. Commun.*, 2014, **5**, 1–9.
15 B. Senyuk, N. Behabtu, A. Martinez, T. Lee, D. E. Tsentalovich, G. Ceriotti, J. M. Tour, M. Pasquali and I. I. Smalyukh, *Nat. Commun.*, 2015, **6**, 1–7.
16 C. R. Gautam, C. S. Tiwary, L. D. Machado, S. Jose, S. Ozden, S. Biradar, D. S. Galvao, R. K. Sonker, B. C. Yadav, R. Vajtai and P. M. Ajayan, *RSC Adv.*, 2016, **6**, 87888–87896.
17 X. Duan, M. Wang, D. Jia, N. Jing, Z. Wu, Z. Yang, Z. Tian, S. Wang, P. He, Y. Wang and Y. Zhou, *Mater. Sci. Eng., A*, 2014, **607**, 38–43.
18 C. R. Gautam, A. Gautam, V. K. Mishra, N. Ahmad, R. Trivedi and S. Biradar, *Ceram. Int.*, 2019, **45**, 1037–1048.
19 S. Schlienger, J. Alauzun, F. Michaux, L. Vidal, J. P. Tier, C. Gervais, F. Babonneau, S. Bernard, P. Miele and J. B. Parra, *Chem. Mater.*, 2012, **24**, 88–96.
20 D. Liu, W. Lei, S. Qin and Y. Chen, *Sci. Rep.*, 2014, **4**, 1–5.
21 M. Pacella, P. W. Butler-Smith, D. A. Axinte and M. W. Fay, *Diamond Relat. Mater.*, 2015, **59**, 62–68.
22 P. B. Mirkarimi, K. F. McCarty and D. L. Medlin, *Mater. Sci. Eng., R*, 1997, **21**, 47–100.
23 G. R. Bhimanapati, M. Wetherington, S. Mahabir and J. A. Robinson, *2D Mater.*, 2016, **3**, 1–8.
24 M. Kawaguchi, S. Kuroda and Y. Muramatsu, *J. Phys. Chem. Solids*, 2008, **69**, 1171–1178.
25 H. Zhang, H. Yan, X. Zhang, M. J. Reece, J. Liu, Z. Shen, Y. Kan and P. Wang, *Mater. Sci. Eng., A*, 2008, **475**, 92–95.
26 J. Eichler and C. Lesniak, *J. Eur. Ceram. Soc.*, 2008, **28**, 1105–1109.
27 D. L. Cai, Z. H. Yang, X. M. Duan, B. Liang, Q. Li, D. C. Jia and Y. Zhou, *Mater. Sci. Eng., A*, 2015, **633**, 194–199.
28 M. Engler, C. Lesniak, R. Damasch, B. Ruisinger and J. Eichler, *Ceram. Forum Int.*, 2007, **84**, E49–E53.
29 J. Yin, X. Li, J. Zhou and W. Guo, *Nano Lett.*, 2013, **13**, 3232–3236.
30 P. Kumbhakar, A. K. Kole, C. S. Tiwary, S. Biswas, S. Vinod, J. T. Tijerina, U. Chatterjee and P. M. Ajayan, *Adv. Opt. Mater.*, 2015, **3**, 828–835.
31 C. Y. Zhi, Y. Bando, C. C. Tang, H. Kuwahara and D. Golberg, *Adv. Mater.*, 2009, **21**, 2889–2893.
32 A. Siria, P. Poncharal, A. L. Biance, R. Fulcrand, X. Blase, S. T. Purcell and L. Bocquet, *Nature*, 2013, **494**, 455–458.
33 X. Duan, Z. Yang, L. Chen, Z. Tian, D. Cai, Y. Wang, D. Jia and Y. Zhou, *J. Eur. Ceram. Soc.*, 2016, **36**, 3725–3737.
34 D. Liu, J. P. Matinlinna and E. H. N. Pow, *J. Adhes. Sci. Technol.*, 2012, **26**, 1249–1265.

35 E. K. Sichel, R. E. Miller, M. S. Abrahams and C. J. Buiocchi, *Phys. Rev. B: Solid State*, 1976, **13**, 4607–4611.
36 A. Simpson and A. D. Stuckes, *J. Phys. C: Solid State Phys.*, 1971, **4**, 1710–1718.
37 V. L. Solozhenko, A. G. Lazarenko, J. P. Petitet and A. V. Kanaev, *J. Phys. Chem. Solids*, 200, **62**, 1331–1334.
38 K. Watanabe, T. Taniguchi and H. Kanda, *Nat. Mater.*, 2004, **3**, 404–409.
39 K. Watanabe, T. Taniguchi and H. Kanda, *J. Cryst. Growth*, 2007, **303**, 525–529.
40 T. G. Kim, H. Shin and D. W. Lim, *Adv. Funct. Mater.*, 2012, **22**, 2446–2468.
41 M. Sarraf, E. Zalnezhad, A. R. Bushroa, A. M. S. Hamouda, A. R. Rafieerad and B. N. Tabrizi, *Ceram. Int.*, 2015, **41**, 7952–7962.
42 B. Artem and J. S. Kutikovand, *ACS Biomater. Sci. Eng.*, 2015, **1**, 463–480.
43 I. Denry and J. R. Kelly, *Dent. Mater.*, 2008, **24**, 299–307.
44 D. Golberg, Y. Bando, Y. Huang, T. Terao, M. Mitome, C. Tang and C. Zhi, *ACS Nano*, 2010, **4**, 2979–2993.
45 Y. Pan, K. F. Huo, Y. M. Hu, J. J. Fu, Y. N. Lu, Z. D. Dai, Z. Hu and Y. Chen, *Small*, 2005, **1**, 1199–1203.
46 Y. Yu, H. Chen, Y. Liu, V. S. J. Craig, C. Wang, L. H. Li and Y. Chen, *Adv. Mater. Interfaces*, 2015, **2**, 1400267–1400276.
47 C. R. Gautam, C. S. Tiwary, S. Jose, G. Brunetto, S. Ozden, S. Vinod, P. Raghavan, S. K. Biradar, D. S. Galvao and P. M. Ajayan, *ACS Nano*, 2015, **9**, 12088–12095.
48 P. Fabbri, C. Piconi, E. Burresi, G. Magnani, F. Mazzanti and C. Mingazzini, *Dent. Mater.*, 2014, **30**, 138–142.
49 M. Fornabaio, P. Palmero, R. Traverso, C. Esnouf, H. Reveron, J. Chevalier and L. Montanaro, *J. Eur. Ceram. Soc.*, 2015, **35**, 4039–4049.
50 H. Reveron, M. Fornabaio, P. Palmero, T. Furderer, E. Adolfsson, V. Lughi, A. Bonifacio, V. Sergo, L. Montanaro and J. Chevalier, *Acta Biomater.*, 2017, **48**, 423–432.
51 C. R. Gautam, D. Chakravarty, A. Gautam, C. S. Tiwary, C. F. Woellner, V. K. Mishra, N. Ahmad, S. Ozden, S. Jose, S. Biradar, R. Vajtai, R. Trivedi, D. S. Galvao and P. M. Ajayan, *ACS Omega*, 2018, **3**, 6013–6021.
52 S. Pilathadka, D. Vahalova and T. Vosahlo, *Prague Med. Rep.*, 2007, **108**, 5–12.
53 J. D. Helmer and T. D. Driskell, *Research on bioceramics, symposium on use of ceramics as surgical implants*, Clemson University, South Carolina, USA 1969.
54 S. Ban, *Japanese Dental Science Review*, 2008, **44**, 3–21.
55 R. R. Samuel, G. Annadurai and S. R. Kumar, *Drug Chem. Toxicol.*, 2019, **42**, 104–111.
56 M. Mishra, S. Debabrat, E. Basanti, S. Swetapadma, P. Unnikannan and D. Priyabrat, *J. Nanopart. Res.*, 2017, **19**, 282–294.
57 S. A. Pappus and M. Mishra, *Adv. Exp. Med. Biol.*, 2018, **18**, 311–322.
58 B. K. Barik and M. Mishra, *Nanotoxicology*, 2019, **13**, 258–284.
59 M. Mishra and B. K. Barik, *Teratogen. Test.*, 2018, vol. 1797, pp. 277–298.
60 L. M. S. Ansaloni and E. M. B. De Sousa, *Mater. Sci. Appl.*, 2013, **4**, 22–28.
61 C. Kizilkaya, Y. Mulazim, M. V. Kahraman, N. K. Apohan and A. Gungor, *J. Appl. Polym. Sci.*, 2012, **124**, 706–712.
62 P. M. Sudeep, S. Vinod, S. Ozden, R. Sruthi, A. Kukovecz, Z. Konya, R. Vajtai, M. R. Anantharaman, P. M. Ajayan and T. N. Narayanan, *RSC Adv.*, 2015, **5**, 93964–93968.
63 E. Aradi, S. R. Naidoo, D. G. Billing, D. Wamwangi, I. Motochi and T. E. Derry, *Nucl. Instrum. Methods Phys. Res., Sect. B*, 2014, **331**, 140–143.
64 C. C. Tang, Y. Bando, Y. Huang, C. Zhi and D. Golberg, *Adv. Funct. Mater.*, 2008, **18**, 3653–3661.
65 A. Cabanas, J. A. Darr, E. Lester and M. Poliakoff, *J. Mater. Chem.*, 2001, **11**, 561–568.
66 R. V. Gorbachev, I. Riaz, R. R. Nair, R. Jalil, L. Britnell, B. D. Belle, E. W. Hill, K. S. Novoselov, K. Watanabe, T. Taniguchi, A. K. Geim and P. Blake, *Small*, 2011, **7**, 465–468.
67 A. J. R. Bauer, ZrO_2 Phase identification with Raman spectroscopy, *Application Note Raman-020*, 2018, vol. A4, pp. 01–03.
68 P. Barberis, T. Merle-Mrjean and P. Quintard, *J. Nucl. Mater.*, 1997, **246**, 232–243.
69 T. Merle, R. Guinebretiere, A. Mirgorodsky and P. Quintard, *Phys. Rev. B: Condens. Matter Mater. Phys.*, 2002, **65**, 144302–144306.
70 S. Vasanthavel, B. Derby and S. Kannan, *Dalton Trans.*, 2017, **46**, 6884–6893.
71 S. Vasanthavel and S. Kannan, *J. Am. Ceram. Soc.*, 2016, **99**, 1212–1220.
72 R. Udaykiran, S. Vasanthavel and S. Kannan, *Cryst. Growth Des.*, 2015, **15**, 4075–4086.
73 S. Vasanthavel and S. Kannan, *J. Am. Ceram. Soc.*, 2014, **97**, 3774–3780.
74 W. W. Lei, D. Portehault, D. Liu, S. Qin and Y. Chen, *Nat. Commun.*, 2013, **4**, 1–7.
75 W. W. Lei, D. Portehault, R. Dimova and M. Antonietti, *J. Am. Chem. Soc.*, 2011, **133**, 7121–7127.
76 C. Devallencourt, J. M. Saiter, A. Fafet and E. Ubrich, *Thermochim. Acta*, 1995, **259**, 143–151.
77 Y. Liu, Y. Wang, S. Zhou, S. Lou, L. Yuan, T. Gao, X. Wu, X. Shi and K. Wang, *ACS Appl. Mater. Interfaces*, 2012, **4**, 4913–4920.
78 R. A. Farah, M. V. Swain, B. K. Drummond, R. Cook and M. Atieh, *J. Dent.*, 2010, **38**, 50–58.
79 L. Chen, Y. H. Huang, Y. J. Wang, H. F. Shen, J. C. Rao and Y. Zhou, *Mater. Sci. Eng., A*, 2013, **573**, 106–110.
80 W. Xue, B. V. Krishna, A. Bandyopadhyay and S. Bose, *Acta Biomater.*, 2007, **3**, 1007–1018.
81 S. Bose, M. Roy and A. Bandyopadhyay, *Trends Biotechnol.*, 2012, **30**, 546–554.
82 C. R. Gautam, S. Kumar, V. K. Mishra and S. Biradar, *Ceram. Int.*, 2017, **43**, 14114–14121.
83 S. Tarafder, V. K. Balla, N. M. Davies, A. Bandyopadhyay and S. Bose, *J. Tissue Eng. Regener. Med.*, 2013, **7**, 631–641.
84 D. Chakravarty, C. S. Tiwary, C. F. Woellner, S. Radhakrishnan, S. Vinod, S. Ozden, P. A. D. Autreto,

S. Bhowmick, S. Asif, S. A. Mani, D. S. Galvao and P. M. Ajayan, *Adv. Mater.*, 2016, **2**, 8959–8967.

85 C. D. Nichols, J. Becnel and U. B. Pandey, *J. Visualized Exp.*, 2012, **61**, 01–05.

86 D. Sabat, A. Patnaik, B. Ekka, P. Dash and M. Mishra, *Physiol. Behav.*, 2016, **167**, 76–85.

87 S. Priyadarsini, S. K. Sahoo, S. Sahu, S. Mukherjee, G. Hota and M. Mishra, *Environ. Sci. Pollut. Res.*, 2019, 1–15.

88 M. Ahamed, R. Posgai, T. J. Gorey, M. Nielsen, S. M. Hussain and J. J. Rowe, *Toxicol. Appl. Pharmacol.*, 2010, **242**, 263–269.

89 E. Baeg, K. Sooklert and A. Sereemaspun, *Nanomaterials*, 2018, **8**, 824.

90 N. A. N. Johnson, Y. Wang, Z. Zeng, G. D. Wang, Q. Yao and K. P. Chen, *J. Asia-Pac. Entomol.*, 2019, **22**, 398–403.

91 M. Mishra, D. Sabat, B. Ekka, S. Sahu, P. Unnikannan and P. Dash, *J. Nano Res.*, 2017, **19**, 282.

92 M. Telonis-Scott, A. A. Hoffmann and C. M. Sgro, *Mol. Ecol.*, 2011, **20**, 2100–2110.

93 A. Takahashi, K. Takahashi, R. Ueda and T. T. Shimizu, *Genetics*, 2007, **177**, 1233–1237.

94 Y. Sekine, S. Takagahara, R. Hatanaka, T. Watanabe, H. Oguchi, T. Noguchi, I. Naguro, K. Kobayashi, M. Tsunoda and T. Funatsu, *J. Cell Sci.*, 2011, **124**, 3006–3016.

